Analysis of Episodic Atmospheric Mercury Oxidation in a Remote Continental Atmosphere

A THESIS

Presented to

The Faculty of the Environmental Studies Program

Colorado College

In Partial Fulfillment of the Requirements for the Degree

Bachelor of Arts in Environmental Science

By

Eleanor Derry

May 2023

Lynne Gratz

Associate Professor of Environmental Science

Table of Contents

Abstract

Mercury is a global pollutant and neurotoxin that bioaccumulates within food chains and can cause adverse health effects with exposure. Although elemental mercury can persist in the atmosphere for months, it can also undergo oxidation chemistry to a more water soluble form that is readily removed from the atmosphere and introduced into ecosystems. However, the chemical mechanisms for mercury oxidation are not well understood. During the spring and summer seasons of 2021 and 2022, continuous measurements of oxidized and elemental mercury, meteorology, trace gases, and aerosol properties were collected at the high elevation Storm Peak Laboratory in Steamboat Springs, Colorado to investigate the origins of atmospheric oxidized mercury and the conditions under which oxidation occurs in a continental environment. We examined this dataset for multi-day periods in which oxidized mercury was at least one standard deviation above the seasonal mean for spring and summer. We generated descriptive statistics and correlation coefficients of meteorological and chemical tracers to examine these multi-day events for air mass composition. We also ran HYSPLIT 10-day back trajectories every six hours using GDAS input meteorological data at 1000 m AGL to examine air mass origins. We then categorized the events based on similarities in composition and transport into three types: Clean Air Events, Elevated Ozone Events, and Combustion Tracer Influenced Events. During the identified episodes, hourly-averaged oxidized mercury concentrations ranged from 121 ± 25 pg/m^3 to 198 ± 26 pg/m^3. Across most events, oxidized mercury was significantly anticorrelated with elemental mercury and relative humidity, and relative humidity remained below 40%, suggesting the occurrence of in-situ oxidation in dry air masses potentially of free tropospheric origin. These results validate and expand upon earlier work at SPL and will be used to further study the underlying chemistry for atmospheric mercury oxidation.

1. Introduction

Mercury (Hg) is a global scale pollutant that can be emitted to the atmosphere from both natural and anthropogenic sources. Humans have altered the Hg cycle through industrial development and land use practices that have increased atmospheric Hg concentrations and altered Hg reservoir distributions (Swartzendruber et al., 2006). Mercury is a neurotoxin that can cause harm to living organisms at high enough concentrations, however at ambient levels Hg is below the threshold at which health impacts can be measured (Lyman et al., 2020). Mercury can methylate in aquatic and marine ecosystems, where it becomes a bioaccumulative neurotoxin (Driscoll et al., 2013). Given its impact on human health, international efforts have been made to reduce anthropogenic Hg emissions. While these have largely been successful, significant gaps remain in the current understanding of atmospheric Hg chemical processes, which must be studied in order to better inform policy and technological development.

Overexposure to Hg can cause a variety of health issues, including neurological and neuromuscular changes, decline in cognitive processing, kidney effects, respiratory failure, and death (EPA, 2022), and young children and people of childbearing age are at the highest risk for Hg poisoning (Selin, 2009). The most common way for Hg to enter human systems is through consumption of contaminated fish, therefore communities that rely on marine ecosystems for the majority of their dietary needs are disproportionately harmed by Hg (Driscoll et al., 2013). In the U.S., 3 to 15% of people of childbearing age exceed the EPA reference dose of Hg (0.1 μg Hg/kg body weight per day) and 15% of children are exposed to levels of Hg that are associated with neurological harm in-utero (EPA, 2022; Driscoll et al., 2013). Additionally, the Environmental Protection Agency (EPA) found that race and income had a statistically significant effect on the median blood Hg level of people with uteruses in the U.S. (EPA, 2022).

The event that shifted international public attention to the risks of Hg was in Minamata Bay, Japan, where hundreds of people in the local community were poisoned by Hg-contaminated industrial wastewater released into the bay. This public health crisis led to efforts to set international Hg standards, culminating in the United Nations signing the Minamata Convention on Mercury in 2013. The convention introduced controls and reductions on anthropogenic processes that emit Hg, regulated storage and disposal of waste from mining industries, expectations for trade and policy, and the establishment of improved healthcare systems for those impacted by Hg (United Nations, 2022). In the U.S., declining trends in atmospheric Hg concentrations can be partially attributed to the 1970 passage of the Clean Air Act and its later amendments that established standards to mitigate anthropogenic Hg emissions (NOAA). Throughout the 1990s, the EPA introduced regulations on the disposal of Hg-containing products and trace metal and particulate matter emissions from industrial and commercial solid waste incinerators (EPA, 2022). In 2008, the U.S. passed the Mercury Export Ban to limit Hg in domestic markets, and in 2011, the EPA issued the Mercury and Air Toxic Standards (MATs) to reduce the emission of toxic air pollutants from coal and oil-fired power plants (EPA, 2022).

Improved emission controls have led to a decline in ambient Hg concentrations. In the 1990s, global ambient Hg concentrations were estimated to be approximately 20x pre-industrial levels, but have declined in the last 30 years due to regulation, such that in 2002, ambient concentrations were estimated to be 11x preindustrial conditions (Schuster et al., 2002). More recent studies have demonstrated that background Hg concentrations were decreasing at a rate of 1.4% per year from the 1990s (Lyman et al., 2020). While these studies show that globally,

background ambient Hg concentrations are declining, local conditions vary significantly due to variations in urban and industrial conditions (Driscoll et al., 2013).

The atmosphere is a key reservoir in the biogeochemical cycle of Hg, however concentrations are not evenly globally distributed. The atmosphere is considered to be a minor reservoir of Hg (~5 GT) compared to soil (1,450 GT) and marine ecosystems (280 GT), but it acts as a key component to global Hg dispersion (Obrist et al., 2018). Natural emitters of Hg include volcanic eruptions and geothermal processes, which contribute 3,600 to 5,300 tons per year, and ocean surfaces are estimated to re-emit 36% of deposited Hg to the atmosphere (Sundseth et al., 2010). By contrast, anthropogenic Hg sources contribute approximately 8 GT per year to the atmosphere (Obrist et al., 2018). The majority of anthropogenic emissions come from coal powered combustion and artisanal gold mining. Relative anthropogenic sources of Hg are shown in Figure 1.

Recent studies have found that from 2010 to 2015, global background terrestrial elemental mercury (Hg^0) concentrations varied spatially. In the northern hemisphere, concentrations ranged from 1.5 to 1.7 ng/m^3, and in the southern hemisphere they ranged from 1.0 to 1.3 ng/m^3 due to a higher concentration of urban areas and greater anthropogenic emissions in the Global North (Sprovieri et al., 2016; Mao et al., 2016). Additionally, Hg species exhibit vertical spatial variability with altitude. Elemental mercury is typically well mixed in the boundary layer (BL), while oxidized mercury (Hg^{II}) has been shown to increase in concentration with elevation, most notably in the free troposphere (FT) (Faïn et al., 2009). Flight-based studies have also demonstrated that Hg^{II} concentrations are higher in the clean, dry air of the FT (Shah et al., 2016). In addition, high elevation research facilities are able to take stationary measurements

of the interplay between the PBL and the FT regarding the effect of meteorology and air mass chemical composition on speciated Hg compounds (Faïn et al., 2009; Timonen et al., 2013).

In the atmosphere, Hg exists as gaseous Hg^0, gaseous Hg^{II}, and particulate-bound mercury (PBM) (Faïn et al., 2009). Elemental mercury has a lifetime in the atmosphere on the scale of months, making it a global pollutant. This form of Hg also has low reactivity and water solubility, allowing it to undergo long-range transport. Oxidized mercury however, is much more reactive and water soluble, resulting in an atmospheric lifetime on the scale of days to a week in the BL (Lyman et al., 2020). Thus, when Hg^0 undergoes oxidation to form Hg^{II}, it is much more readily deposited into ecosystems, and can therefore bioaccumulate into food webs (Lyman et al., 2007).

The chemical oxidation mechanisms and fate of Hg in the atmosphere are complex and not well understood. Previous studies have indicated multiple possible major oxidants of Hg in the atmosphere. The most recent studies have suggested that Hg oxidation occurs in the FT, and the primary oxidants are halogens such as atomic bromine (Br), and the hydroxyl radical (OH) (Dibble et al., 2020). Oxidation in the FT is thought to be driven by a two-step mechanism approximated in Figure 2 (Shah et al., 2021). The two-step halogen chemistry is summarized below, where radicals Y = Br, Cl, and OH, Z = another radical, and M = a non-reactive molecule (Shah et al., 2021).

$$Hg^0 + Y + M \leftrightarrow YHg^I + M \qquad (R1)$$

$$YHg^I + Z + M \rightarrow YHg^{II}Z + M \qquad (R2)$$

Many components of this chemical process are still uncertain. Part of this uncertainty comes from limitations in commercial instrument and measurement precision, which underestimate Hg^{II} concentrations (Lyman et al., 2020). In this study, we employ new Hg

instrumentation with higher confidence that Hg^{II} concentrations are being more accurately recorded (Lyman et al., 2020). Data was collected at Storm Peak Laboratory (SPL) in Steamboat Springs, Colorado during two six-month periods, spring and summer 2021 and 2022. SPL is a well-established high elevation site measuring a remote continental atmosphere, where both anthropogenic sources and transitions between the BL and FT have been documented (Faïn et al., 2009; Obrist et al., 2018). This analysis examines meteorology and air mass composition and transport during events of elevated Hg^{II} from spring and summer 2021 and 2022 to better understand the conditions under which Hg oxidation occurs in a continental atmosphere.

2. Methods:

2.1 Site Description:

The data used in this study were collected at Storm Peak Laboratory (SPL; 3220 m AMSL; 40.455 N, 106.744 W) in Steamboat Springs, CO. SPL is a permanent high elevation research facility within the Rocky Mountains along the Continental Divide. The site is ideally located to measure a remote continental atmosphere and the transitions between the BL and the free troposphere (FT). SPL receives prevailing westerly winds, creating a clear upwind fetch (Faïn et al., 2009), and is located east of the agricultural Yampa Valley and approximately 19 km from downtown Steamboat Springs (Figure 3).

2.2 Mercury Instrumentation and Data Collection:

Atmospheric Hg concentration measurements were taken from March 12, 2021 to October 11, 2021 and March 3, 2022 to September 29, 2022; this study will focus specifically on the data from March 13, 2021 to September 15, 2021 and March 3, 2022 to September 15, 2022

in order to encompass two full seasons from each year. In the 2021 dataset, data were unavailable from May 12, 2021 to June 6, 2021, June 29, 2021 to July 9, 2021, and August 2 to 10, 2021. In 2022, Hg data was unavailable from June 27, 2022 to July 1, 2022 and August 16 to 23, 2022. Elemental mercury and Hg^{II} were measured using the Utah State University dual-channel Hg measurement system with a Tekran 2527 X mercury vapor analyzer. The dual-channel system functions by pulling ambient air through the main inlet at a rate of 8 standard L/minute into a weatherproof box containing a pyrolyzer and a pair of in-series cation-exchange membranes. The pyrolyzer is constructed of quartz, packed with quartz chips, and maintained at a temperature of 650℃ to convert Hg^{II} to Hg^0 such that total Hg is measured ($THg = Hg^{II} + Hg^0$) (Lyman et al., 2020). The cation-exchange membranes captured the Hg^{II}, allowing only the Hg^0 to pass through. At five-minute intervals, a valve switches between the pyrolyzer and the cation-exchange membranes, resulting in a complete set of Hg measurements every ten minutes.

Inlet and sample lines were maintained at a temperature of 110°C to minimize contamination and wall losses. Hg^0 concentrations were reported in ng/m^3, and Hg^{II} was reported in pg/m^3. The dual-channel system was verified for measurement accuracy with a calibrator that injects a known amount of Hg^0, $HgBr_2$, and $HgCl_2$ into the inlet on a weekly basis. The calibration process is a key difference between the dual-channel analyzer and commercially-available instruments, such as the KCl-denuder based systems that are shown to under-report Hg^{II} concentrations and are not routinely calibrated for Hg^{II}. Elemental mercury vapor injections on the Tekran 2537X were performed every 6 to 8 weeks to verify the permeation rate of the internal calibration source (Zwecker, 2021).

2.3 Criteria Gas and Meteorological Measurements

Criteria gases and meteorological variables that are continuously measured at SPL were used in this study. Meteorological data was measured on the roof of SPL at a height of 10 m above ground level (AGL) at a five-minute time resolution, which was quality-assured and made publicly available by MesoWest (mesowest.utah.edu). Atmospheric composition measurements used in this study consisted of ozone (O_3; Thermo Model 49i analyzer; 1 min), nitrogen oxides (NO_x; Thermo Model 42i NO-NO2-NOx analyzer; 1 min), sulfur dioxide (SO_2; Thermo Model 43i analyzer; 1 min), carbon monoxide (CO; Teledyne model 300E) which was logged every 10 minutes in 2021 and then every 1 minute in 2022, and aerosol PM1 and PM10 scattering (PM_1 σ_{sp}; TSI model 3562 Nephelometer; 1 min). All the meteorological and gas data were collected continuously throughout the study period, except for CO, where measurements began on July 7, 2021, and were taken continuously thereafter.

2.4 Statistical Analysis

The data was averaged to 1-hour intervals corresponding to the top of each hour to compare all the criteria on the same time step. The dataset was divided seasonally into spring (March, April, May) and summer (June, July, August, including the first two weeks of September) for each year in order to account for seasonal variation in atmospheric Hg concentrations. Past work has shown that trans-Pacific transport as well as events influenced by the Upper Troposphere/Lower Stratosphere (UT/LS) occur in springtime, while summertime air masses at SPL are frequently impacted by biomass burning (Obrist et al., 2018), and may see less of the springtime meteorological behaviors, therefore seasonal division best accounted for these regime changes. Descriptive statistics and Pearson correlation coefficients were calculated using

Excel v16.65 and IBM SPSS Statistics v28.0.0.0. In this study, significance is defined as $p < 0.05$.

2.5 Identification of Events of Elevated Oxidized Mercury

We calculated the mean Hg^{II} and Hg^{0} concentrations for each season and defined an event of elevated Hg^{II} as a period when Hg^{II} concentrations were at least one standard deviation above the seasonal mean (mean + 1 σ) for a minimum of 24 hours. These parameters expanded the total number of events beyond the six initially analyzed by Zwecker (2021) to capture a broader range of events during which oxidation could be occurring. In order to understand the origins of the air masses in which elevated concentrations of Hg^{II} were found, we classified the events based on similarities across events in calculated means, maxima, minima, significant Pearson correlations between Hg^{II} and other trace gases and meteorology, and air mass trajectories. This methodology is similar to that used by Timonen et al. (2013) for characterizing the origins of Hg^{II} to the high-elevation Mount Bachelor Observatory in Bend, OR.

2.5.1 HYSPLIT Air Mass Trajectories

We modeled air mass trajectories using the National Oceanic and Atmospheric Administration's (NOAA) Hybrid Single-Particle Lagrangian Integrated Trajectory (HYSPLIT) model, specifically with the GDAS model dataset (HYSPLIT, Stein et al. 2015). The model ran a 10-day backwards ensemble trajectory to visualize the spatial pathways, both horizontal and vertical, of the air masses of interest to SPL. We ran the model using multiple different end times throughout each event to create a representative trajectory for each air mass and gain a better understanding of the transport pathway. The ensemble trajectory runs multiple trajectories from

the same end time and location, but for a set of meteorological conditions offset from the center point. Using the GDAS model, SPL was estimated to be at 1000 m AGL to achieve a starting pressure comparable to a typical atmospheric pressure at the site. The endpoint of the trajectories was set at 40.455 N, 106.744 W.

2.5.2 Trajectory Meteorological Data

In conjunction with the HYSPLIT ensemble trajectory models, we also analyzed the meteorology of the air masses of interest over the 10-day period prior to arriving at SPL. Using the HYSPLIT GDAS model numerical data, we examined the relative humidity and precipitation along each 10-day trajectory corresponding to Hg^{II} events in comparison with the vertical height of the air mass as it approached SPL and compared the meteorology across all events.

3. Results and Discussion:

3.1 Data Overview

In the 2021 data collection period, from March 12, 2021 to September 15, 2021, seasonal mean Hg^0 and Hg^{II} concentrations at SPL were 1.3 ± 0.1 ng/m^3 and 80 ± 50 pg/m^3 for springtime and 1.2 ± 0.1 ng/m^3 and 116 ± 39 pg/m^3 for summertime, respectively. Elemental mercury concentrations ranged from 1.0 to 2.1 ng/m^3 in spring 2021 and 0.9 to 2.4 ng/m^3 in summer. The maximum Hg^{II} concentrations were 520 pg/m^3 in spring and 253 pg/m^3 in summer. In 2022, from March 3, 2022 to September 15, 2022, seasonal mean Hg^0 and Hg^{II} concentrations were 1.3 ± 0.1 ng/m^3 and 80 ± 40 pg/m^3 in springtime and 1.2 ± 0.1 ng/m^3 and 84 ± 39 pg/m^3 for summertime. Concentrations of Hg^0 ranged from 0.8 to 1.7 ng/m^3 in springtime and 0.9 to 1.7 ng/m^3 in summertime, and maximum concentrations of Hg^{II} were 293 pg/m^3 in spring and 197 pg/m^3 in

summer. Summary statistics of seasonal Hg, meteorology, and criteria gases are shown in Tables 1-4, and Figures 4 and 5 depict both Hg species' hourly concentrations over each year's study period.

Broadly, the mean seasonal Hg concentrations do not differ greatly between 2021 and 2022, except for the summer Hg^{II} mean, which was considerably lower in 2022 than 2021. The mean seasonal Hg^0 concentrations were not statistically different within the precision level of the instrument. The mean spring concentrations of Hg^{II} from each year were not significantly different, however the summer Hg^{II} mean concentrations were significantly statistically different, where $p < 0.001$. A previous study conducted at SPL by Faïn et al. (2009) on events of enhanced Hg^{II} concentrations found the mean concentration of Hg^0 to be 1.6 ng/m^3 and the mean concentration of Hg^{II} to be 20 pg/m^3 for a study period lasting from April 28 to July 1, 2008. Elemental mercury concentrations in this study were much lower, which aligns with other studies that have reported consistent declines in background Hg^0 over the past several decades. Meanwhile, the concentrations of Hg^{II} reported in this study are much higher, indicating a higher instrument precision in the dual-channel system than commercially available Hg instrumentation. Mean and maximum Hg^{II} concentrations were found to be four to five times higher than earlier work.

3.2 Elevated Oxidized Mercury Events

In broadening the methodologies developed by Zwecker (2021) and including the 2022 Hg spring and summer dataset in our analysis, we found 18 events in addition to the four previously analyzed in the 2021 data. This expansion led to a more extensive scope and understanding of the varied conditions under which in situ Hg oxidation can occur in the atmosphere.

Additionally, analyzing two years of data allowed us to examine both seasonal and annual Hg patterns across multiple years using the dual-channel system.

In 2021, we identified nine periods where Hg^{II} concentrations were at least one standard deviation above the seasonal mean for a sustained period. The event cutoff (mean + 1σ) for spring was 130 pg/m^3, and 155 pg/m^3 for summer. Three of the events occurred in springtime, and six in summer, and are outlined in Table 5. During the 2022 study period, we identified thirteen additional events using the same methodology (seasonal mean + 1σ). The Hg^{II} cutoff was 120 pg/m^3 for springtime and 123 pg/m^3 for summertime in 2022. Six of these events occurred in spring, and seven occurred in summer, as shown in Table 6. The 2022 Hg^{II} cutoffs were much lower than those in 2021 because the seasonal means were lower, leading to a larger group of events from the 2022 study period than the previous year.

3.3 Event Characterization

After identifying and analyzing the properties of each event, we characterized events based on similarities in their composition and transport patterns. For 18 of the events, Hg^{II} was significantly anticorrelated with Hg^0, across 13 of these events, there was a statistically significant anticorrelation between Hg^{II} and relative humidity, and in all but Event 20, relative humidity dropped below 40% for the majority of the time period. The strong anticorrelations between Hg^{II} and Hg^0 in the majority of the selected events indicate that Hg oxidation was occurring in the atmosphere and is a source of Hg^{II}, as opposed to through direct emission of Hg^{II} at SPL in the measured air masses.

Oxidized mercury had varied significant correlations with trace gases and aerosol scattering across all 22 events, which are described in Table 7 for the 2021 study period and

Table 8 for 2022. Summary statistics for each of the events discussed in detail in this study are shown in Table 9. Using relative humidity, precipitation, and air mass height over the 10 days prior to arrival at SPL for one HYSPLIT trajectory per event, it was determined that in each case, no precipitation had occurred for at least five days prior to arrival of the air mass at SPL. This approach was limited in its ability to fully represent the meteorology occurring along the trajectory of the air mass as we only examined one possible trajectory. Three ensemble trajectories from varying times for each categorized event are shown in Figure 6. Additionally, the maximum precipitation rate during the 10 day period before the event never exceeded 2.9 mm/hr. In most cases, zero precipitation was measured along the trajectories for any of the events. The relative humidity for the back trajectories varied across the events. In all cases, values were consistently low as the air mass approached SPL.

Based on similarities in the correlation coefficients calculated between Hg^{II} and auxiliary variables, event statistics, meteorology, and transport modeling, we grouped 13 of the events into three categories: Clean Air Events, Elevated Ozone Events, and Combustion Tracer Influenced Events. The remaining events were excluded from further analysis in this study as there were no consistent commonalities in their composition or transport. The characterization approach taken in this study follows to some extent the methods of Timonen et al. (2013), where they analyzed data collected at Mount Bachelor Observatory (MBO) in Bend, Oregon, and defined three categories for events of elevated Hg^{II}: UT/LS influenced events (Swartzendruber et al., 2006), Asian Long-Range Transport (ALRT) events, and MBL influenced events. Figure 7 shows examples of these air mass transport pathways as demonstrated by Timonen et al. (2013) at MBO, which used a similar dataset and approach.

Events not discussed further in this study are 1, 10, 11, 12, 14, 16, 18, 19, and 20. All of these events demonstrated evidence of in situ Hg oxidation, based on strong inverse relationships between Hg^{II} and Hg^{0} and overall low relative humidity values, and therefore warrant continued study to further understand Hg^{II} origins at SPL. However, these events had less in common with others in terms of composition and transport, and are therefore not included in the characterization of events that is discussed in the remainder of Section 3.3.

UT/LS events were defined at MBO by an increase in O_3 concentrations and a positive correlation between Hg^{II} and O_3, as well as a simultaneous decrease in CO concentrations and aerosol scattering (Timonen et al., 2013). In addition to these criteria, we also examined air mass transport using the HYSPLIT GDAS 10 day ensemble backwards trajectories to determine whether the air mass traveled at a high enough elevation in the atmosphere to have UT/LS influence (Timonen et al., 2013). In ALRT events at MBO, Hg^{II} was anticorrelated with Hg^{0} and positively correlated with anthropogenic pollution tracers (CO and O_3), HYSPLIT showed air masses to have traveled over Asia in the 10 days prior to arriving at MBO, and THg/CO and O_3/CO ratios were consistent with previous measurements of Asian pollution plumes at MBO. MBL influenced events were defined by very clean air masses that circled over the Pacific Ocean for at least 10 days prior to arriving at MBO, particularly high Hg^{II} measurements simultaneous to a decrease in CO, aerosol scattering, and O_3 concentrations, as well as O_3 and water vapor mixing ratios that demonstrated influence from the clean subtropical MBL (Timonen et al., 2013).

MBO is ideally positioned to measure with confidence ALRT and MBL events due to its location near to the western coast of North America, so air masses that arrive at MBO are less likely to be influenced by mixing with continental air masses and emission sources. By contrast,

SPL is located over 1000 miles from the Pacific Coast, allowing air masses to mix with continental air masses that have a different composition and properties than the MBL or FT as they travel across the continent. It is therefore more challenging to group the SPL events into conclusive categories with high confidence, due to the higher number of factors influencing air mass composition by the time of arrival at SPL. The geographic differences between these sites meant that none of the events at SPL identified in this study were characterized as having clear influence from ALRT or the MBL. However, finding similarities in the composition and transport of air masses containing elevated concentrations of Hg^{II} furthers our understanding of sources of atmospheric Hg^{II} and conditions under which oxidation occurs.

3.3.1 Clean Air Events

In four events across both years, the particularly low concentrations of criteria gases and aerosol scattering data in comparison to their seasonal means (Tables 1-4) and other event concentrations (Table 9) suggested that Hg oxidation was occurring in very clean, dry air. Events 2, 4, 5, and 15 all showed Hg^{II} significantly anticorrelated with pollution tracers (aerosol scattering, CO, NO_x, O_3, SO_2) and relative humidity, and had no significant positive correlations between Hg^{II} and any pollution tracers. Events 2 and 15 occurred in springtime, while Events 4 and 5 occurred in summertime. Additionally, the event means and maxima for each of these tracers were low compared to their seasonal values. The event means and standard deviations are shown in Table 9.

In Event 2, Hg^{II} was significantly anticorrelated with Hg^0, relative humidity, aerosol PM_1 scattering, O_3, and NO_x, with R values ranging from -0.26 to -0.56. The Hg, meteorology, aerosol PM_1 scattering, and trace gases timeseries for Event 2 are shown in Figure 8. Oxidized mercury

was anticorrelated with Hg^0, O_3, NO_x, SO_2, relative humidity, and aerosol PM_1 scattering during Events 4 and 5. Mercury, meteorology, aerosol PM_1 scattering, and trace gas data for these events are depicted in Figure 9 (Event 4) and Figure 10 (Event 5). Carbon monoxide data was not available for these three events. Oxidized mercury was anticorrelated with relative humidity, aerosol PM_1 scattering, NO_x, SO_2, and CO in Event 15. The timeseries for Hg, meteorology, aerosol PM_1 scattering, and trace gases for Event 15 are shown in Figure 11. The Pearson correlation coefficients for these events are listed in Table 7 (Events 2, 4, and 5) and Table 8 (Event 15). Low relative humidity values (less than 40%) and pollution tracer concentrations across these events indicate that in situ Hg oxidation is likely occurring in the clean, dry air of the Free Troposphere (FT). Mean concentrations of pollution tracers for these events are shown in Table 9.

Previous studies have also noted that Hg oxidation likely occurs in the FT, and in clean, dry conditions. A study conducted at SPL in 2008 found that 40% relative humidity was an indicator that SPL was in the FT and not measuring air from the BL. The data analysis found that low relative humidity was the dominant factor during periods of elevated Hg^{II}, which aligns with the results of this study, indicating that these types of oxidation events were related to tropospheric and stratospheric Hg^0 reservoirs (Faïn et al., 2009). However, the previous study did not note any time periods where Hg^{II} was elevated where there was a simultaneous increase in pollution tracers. As discussed in Section 3.3.3, our study found several events of elevated Hg^{II} indicative of oxidation where there was also an increase in pollution tracer concentrations under various conditions. Overall, the 2008 study found higher concentrations of Hg^0, with a mean of 1.6 ± 0.3 ng/m^3 for the April through July 2008 study period, while the mean Hg^{II} was 20 ± 21 pg/m^3. This study found lower mean Hg^0 concentrations, with seasonal means for both years

ranging from 1.2 ± 0.1 to 1.3 ± 0.1 ng/m^3, reflecting the decline in atmospheric Hg concentrations over the past several decades (Lyman et al., 2020). However, the Hg^{II} measurements from the dual-channel system with the Tekran 2537X Hg vapor analyzer gave higher concentrations that previously reported at SPL, with seasonal means ranging from 79 ± 51 to 120 ± 42 pg/m^3, showing that the dual-channel system has much higher precision in Hg measurements.

An aircraft study in 2013 also found evidence of Hg oxidation in the clean, dry air of the FT. This study measured lower concentrations of Hg^0 at higher altitudes corresponding to the FT (1.02 ± 0.06 ng/m^3) than in the BL, indicating the formation of Hg^{II} from Hg^0 and less influence from continental Hg sources. Mean Hg^{II} concentrations in this study were 0.266 ± 0.038 ng/m^3, and ranged from 0.182 to 0.347 ng/m^3 (Gratz et al., 2015). The durations of these two studies were different, and the aircraft study was able to collect data while moving through the air mass, while this study collected data from a stationary site; however, the mean Hg^0 concentrations from Gratz et al. (2015) are similar to the mean Hg^0 for the selected events in this study. The Hg^{II} event mean concentrations are generally higher at SPL, again indicating the measurement accuracy and magnitude of the improved dual-channel system, but follow the same pattern of increase simultaneous to Hg^0 decrease when in clean, dry air. The event mean Hg^0 and Hg^{II} concentrations are listed in Table 9.

3.3.2 Elevated Ozone Events

Events 3, 6, 7, 8, 9, 13, 17, and 21 all displayed significant positive correlations between Hg^{II} and O_3, but varying relationships with other auxiliary variables. Event 3 occurred in Spring 2021, Events 6, 7, 8, and 9 occurred in Summer 2021, Event 13 took place in Spring 2022, and

Events 17 and 21 occurred in Summer 2022. However, Events 6, 7, and 8 were also defined by air masses with influence from biomass burning, and therefore these events will be discussed in Section 3.3.3. In springtime, Events 3 and 13, Hg^{II} was anticorrelated with Hg^0 and relative humidity and positively correlated with O_3 and aerosol PM_1 scattering. Meteorology and trace gas concentrations are shown for Event 3 in Figure 12. In Event 9, Hg^{II} was anticorrelated with Hg^0 and positively correlated with O_3 and CO, full time series for which are in Figure 13. In Event 17, Hg^{II} was anticorrelated with aerosol PM_1 scattering and positively correlated with O_3, time series for which are shown in Figure 14. In Event 21, Hg^{II} was anticorrelated with Hg^0, relative humidity, and aerosol PM_1 scattering and positively correlated with O_3. Pearson correlation coefficients with p-value significance are shown in Tables 7 and 8.

Events 13 and 21 indicate that the air masses may have been influenced by the UT/LS based on the definition of a UT/LS influenced event MBO by Swartzendruber et al. (2006). In Event 13, Hg^{II} and O_3 both increased for the duration of the event, Hg^0 concentrations decreased simultaneously, aerosol PM_1 scattering remained very low, and CO concentrations dropped in the middle of the event (Figure 15). Event 21 also shows increases in Hg^{II} by approximately 0.05 ng/m^3 and O_3 by approximately 10 ppb, and concurrent decreases in Hg^0 and CO concentrations and PM_1 aerosol scattering (Figure 16), indicating that the air masses in which Hg oxidation is occurring may have had influence from the UT/LS. Backwards ensemble trajectory models using HYSPLIT GDAS suggest that the air masses for these events traveled at a maximum altitude of approximately 8000 m AGL for multiple days before arriving at SPL. A previous aircraft study conducted in 2010 measured Hg in a UT/LS air mass and found that Hg^{II} concentrations were strongly correlated with stratospheric air tracers (O_3 and potential vorticity), while THg and Hg^0 levels were anticorrelated with these tracers. During the strongest event they measured, Hg^{II} was

positively correlated with stratospheric air tracers, and negatively correlated with CO (Lyman and Jaffe, 2011), similar to Events 13 and 21 in this study, indicating that Hg^{II} concentrations increased with stratospheric influence. In the study that first described UT/LS influenced events of Hg oxidation by Swartzendruber et al. (2006), the 95th percentile Hg^{II} concentration was 141 ± 75 pg/m^3, which is within the range of mean Hg^{II} concentrations in the UT/LS events in this study. Their reported O_3, CO, and aerosol scattering also aligned with the measurements in this study, which are shown in Table 9.

The other events that demonstrated positive correlations between Hg^{II} and O_3 did not exhibit all the same characteristics as a UT/LS influenced event (Events 3, 9, and 17). Event 3 took place in Spring 2021, and exhibited a particularly strong anticorrelation between Hg^{II} and Hg^0 (R^2 = 0.91), providing a strong indication that Hg oxidation occurred in this air mass. While there was a significant positive correlation between Hg^{II} and aerosol PM_1 scattering, the event mean for aerosol PM_1 scattering was the same as the Spring 2021 seasonal mean. Event 9 showed a positive correlation between Hg^{II} and CO in contrast to Events 13 and 21, but the mean CO concentration was 170 ± 20 ppb, which was within the standard deviation of the Summer 2021 seasonal mean of 200 ± 90 ppb. This event did not show a significant correlation between Hg^{II} and relative humidity, although relative humidity remained below 40%, and the HYSPLIT ensemble trajectories showed that the air mass traveled as high as 8000 m AGL in the 10 days prior to arriving at SPL, as shown in Figure 6. Event 17 did not display a significant anticorrelation between Hg^{II} and Hg^0 or Hg^{II} and relative humidity, although Hg^{II} increased over one standard deviation above the Summer 2022 mean for the duration of the event, and O_3 increased while aerosol PM_1 scattering decreased. The HYSPLIT trajectories in Figure 6 model

lower transport in the 10 days before the air mass arrived at SPL, so potentially this event was caused by a direct Hg^{II} emission from the continent, rather than an oxidation event.

3.3.3 Combustion Tracer Influenced Events

Events 6, 7, and 8 from Summer 2021 occurred when there were local or regional wildfires around SPL, and therefore smoke in the measured air masses. Biomass burning influence was defined by elevated CO concentrations and aerosol scattering, where CO was greater than 150 ppb, aerosol PM_1 scattering was greater than 30 Mm^{-1}, and aerosol PM_{10} scattering was greater than 35 Mm^{-1} for a minimum of one hour. The presence of overhead smoke was also verified by the NOAA HMS Fire and Smoke product. Although biomass burning events have been shown to volatilize stored Hg as Hg^0 and release it to the atmosphere (McLagan et al., 2021), the Hg^0 means for these three events were comparable to the seasonal Hg^0 mean for Summer 2021 (1.2 ± 0.1 ng/m^3), which indicates that Hg oxidation was occurring given the simultaneous increase in Hg^{II} and anticorrelation between Hg^{II} and Hg^0 in all of these events. Event means are shown in Table 9. Mercury and trace gas concentrations, relative humidity, and aerosol PM_1 scattering values for Event 6 are shown in Figure 17, Event 7 in Figure 18, and Event 8 in Figure 19.

Event 22 displayed enhanced concentrations of combustion tracers (NO_x, SO_2, CO, and aerosol scattering) that coincided with the increase in Hg^{II} and characteristics of an Hg oxidation event at SPL, based on low relative humidity and a significant anticorrelation between Hg^{II} and Hg^0. Oxidized mercury was significantly positively correlated with CO, SO_2, and NO_x during this event (Table 8). Additionally, CO concentrations were particularly elevated during this time period, ranging from 160 to 280 ppb. While these ranges of CO concentrations could be

indicative of a biomass burning event, the aerosol PM_1 scattering remained low, ranging from 2.13 to 6.86 Mm^{-1}, which fall well below the chosen metric for influence from a biomass burning event. Figure 20 shows Hg^0, Hg^{II}, SO_2, NO_x, and CO concentrations and aerosol PM_1 scattering over Event 22. Despite low aerosol scattering measurements at SPL, the Air-Now Tech Navigator showed that overhead smoke was present at SPL during the full timespan of Event 22, as shown in Figure 21, but there were no local fires within 25 km upwind of the lab. There were, however, many active fires in the Pacific Northwest and Idaho at the time, so SPL may have been receiving an aged smoke plume from this region. HYSPLIT 72-hour ensemble trajectories also showed the air mass traveled across the northwestern U.S. in the three days before it arrived at SPL, where fires were present, as shown in Figure 22.

The role of Hg^{II} in biomass burning plumes is not fully understood and is an ongoing area of study. Previous studies have shown that wildfires are an important source of Hg to the atmosphere, but have not reported an increase in Hg^{II} during biomass burning events. A study that examined particulate-bound Hg emissions from wildfires around MBO from 2005 to 2007 in spring, summer, and early fall found that Hg^0 concentrations increased in coincidence with CO and aerosol scattering during biomass burning events, but did not pick up Hg^{II} in the smoke plumes (Finley et al., 2009). An aircraft study with a focus on Hg emissions from biomass burning events in North American forests also found that if Hg^{II} was present in the measured smoke plumes, it was below the detection limit of the instrument, but Hg^0 was above ambient concentrations in the smoke plumes (Friedli et al., 2003). However, the events in this study that occurred during biomass burning events imply that Hg oxidation could be occurring within some smoke plumes. This conclusion is possibly related, in part, to the higher instrument precision of the dual-channel system, that allows for more accurate and higher time resolution Hg^{II}

measurements than previously available, although it is currently unclear whether Hg oxidation occurred because of some attribute of the smoky air mass composition or coincidentally simultaneous to local or regional biomass burning events that brought smoke to SPL.

4. Conclusion

This study examines the composition and transport pathways of air masses in which Hg is undergoing oxidation in a remote continental atmosphere. We identified a range of events that displayed characteristics of Hg oxidation and then characterized 13 of them based on similarities in relative concentrations of chemical species, meteorology, and transport pathways in order to better understand the atmospheric conditions under which oxidation occurs. Overall, we demonstrated that elevated Hg^{II} concentrations were generally driven by oxidation of Hg^{0} in the clean, dry air of the free troposphere. However, we also identified three subsets of general conditions under which oxidation is occurring: Clean Air Events, Elevated Ozone Events, and Combustion Impacted Events.

Clean Air Events were defined by low concentrations of pollution tracers that declined simultaneous to an increase in Hg^{II}. Elevated Ozone Events were designated when Hg^{II} and O_3 concentrations were significantly positively correlated and O_3 concentrations were high in comparison to the seasonal means. Based on transport modeling, it is possible that some of these events were influenced by intrusions of air from the UT/LS, but more analysis is needed to fully understand the origins of these conditions. Combustion Impacted Events were defined by elevated levels of combustion tracers, and verified with overhead smoke analysis. Many of these events occurred under smoky conditions at SPL, due to a combination of local and regional

wildfires. The impacts of biomass burning events on atmospheric Hg^0 and Hg^{II} concentrations is an ongoing area of research, which will further explain the dynamics that create these events.

Results from this study contribute to current understandings of Hg oxidation in a remote continental atmosphere. Additionally, the implementation of the dual-channel system provided Hg measurements that were larger in magnitude and more accurate than commercially available instrumentation. Ongoing and future work can better parameterize the oxidation chemistry that Hg^0 undergoes in the atmosphere to form Hg^{II}, and how technology and policy can limit the harmful impact of Hg on both human and ecosystem health.

Figures:

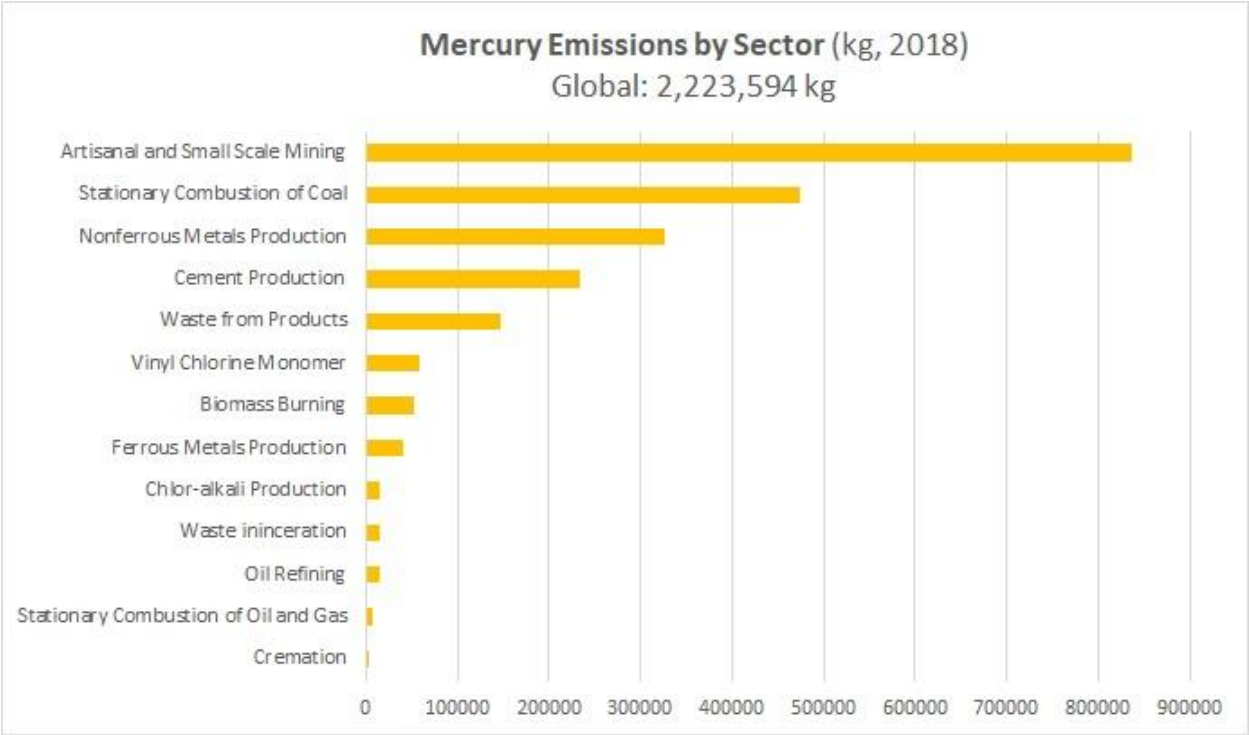

Figure 1: Global Sources of Atmospheric Hg by % as of 2018 (EPA)

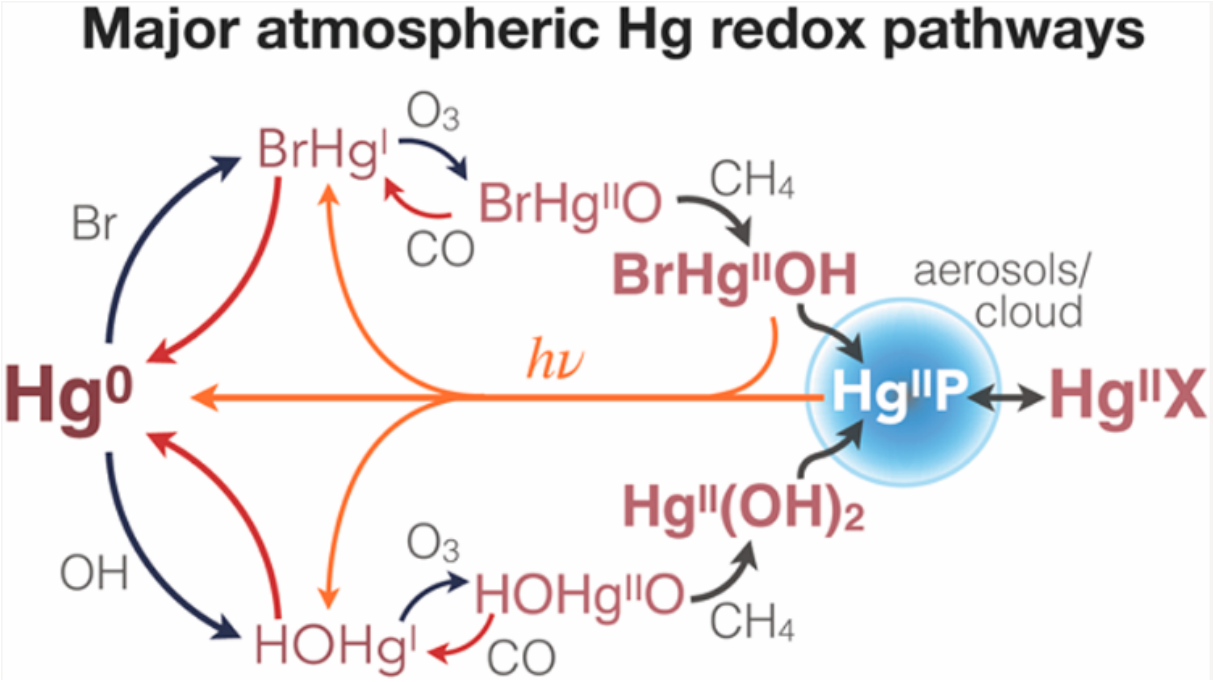

Figure 2: Diagram of Atmospheric Hg Redox Pathways (Shah et al., 2021)

Figure 3: Map of Storm Peak Laboratory in Western Colorado (Google Earth). SPL is at an elevation of 3220 m AMSL.

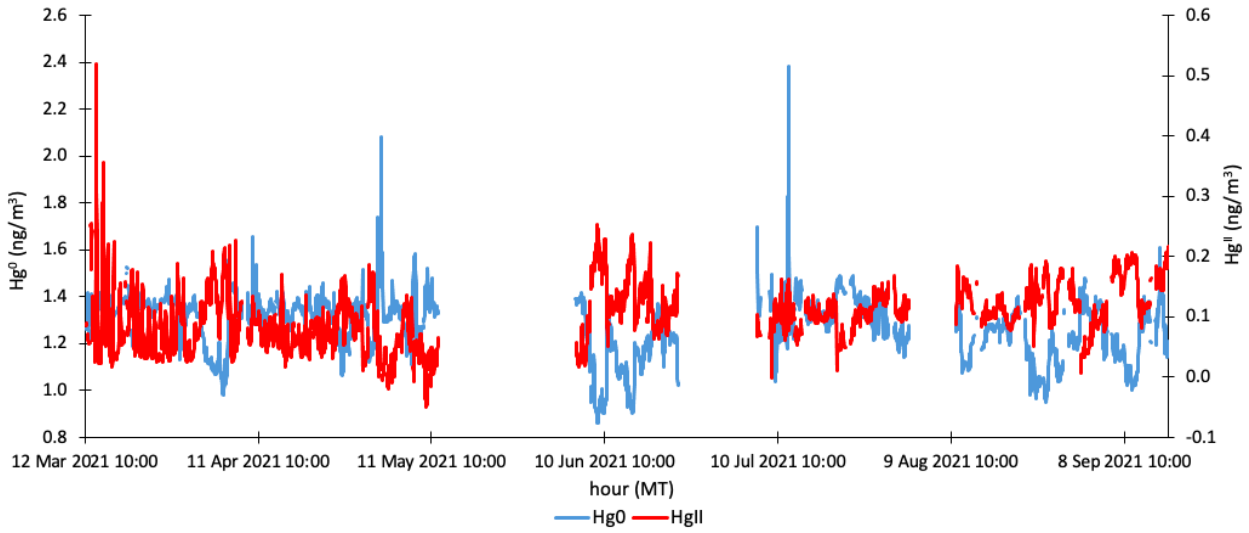

Figure 4: 2021 time series showing Hg^0 and Hg^{II} concentrations at SPL from March 12, 2021 - September 15, 2021.

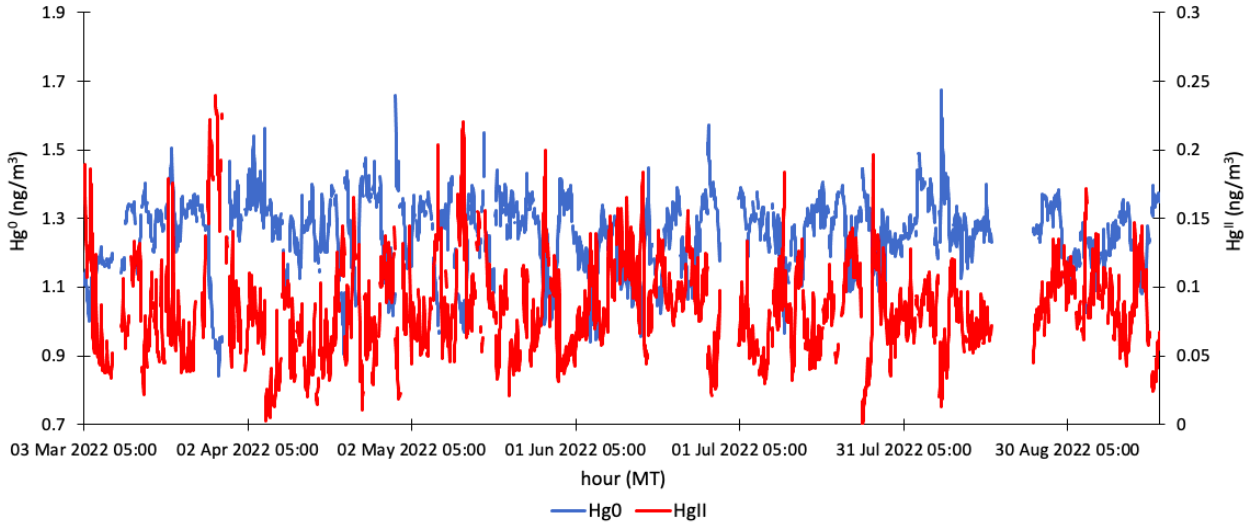

Figure 5: 2022 time series showing Hg^0 and Hg^{II} concentrations at SPL from March 3, 2022 to September 15, 2022. Data gaps are due to instrument recalibration.

Event 2: April 24, 2021 23:00 MST - April 27, 2021 05:00 MST

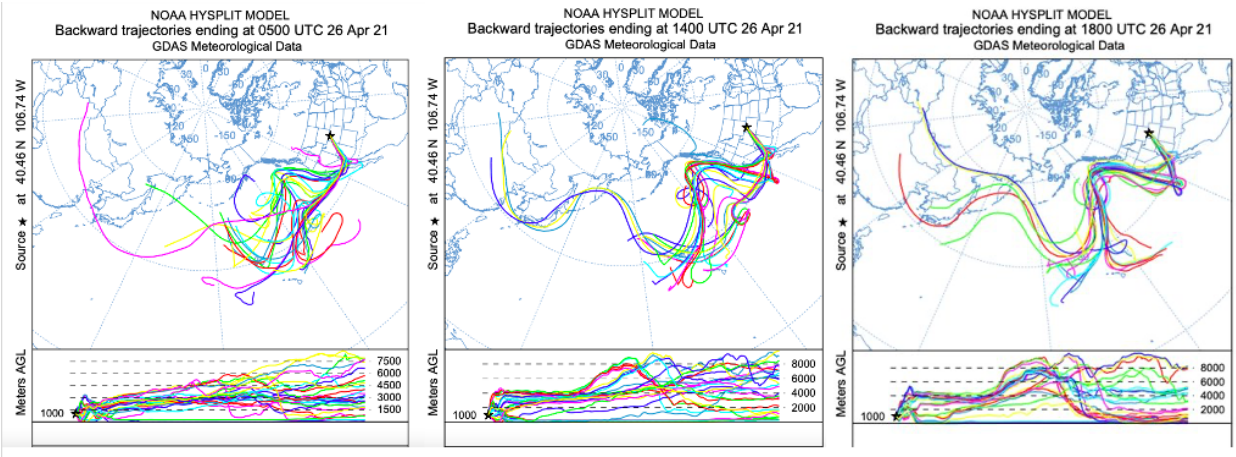

Event 3: April 30, 2021 14:00 MST - May 1, 2021 12:00 MST

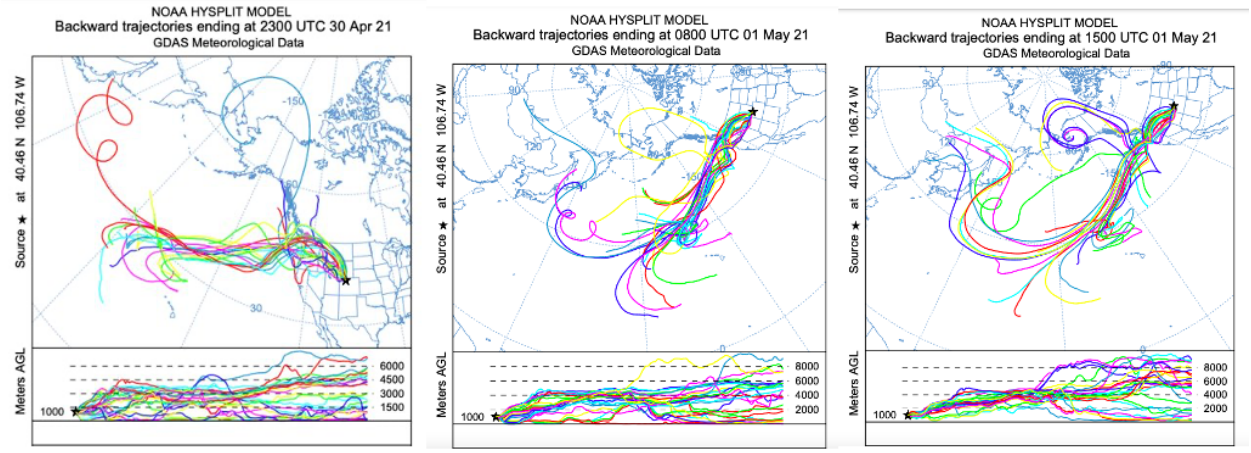

Event 4: June 8, 2021 01:00 MST - June 10, 2021 20:00 MST

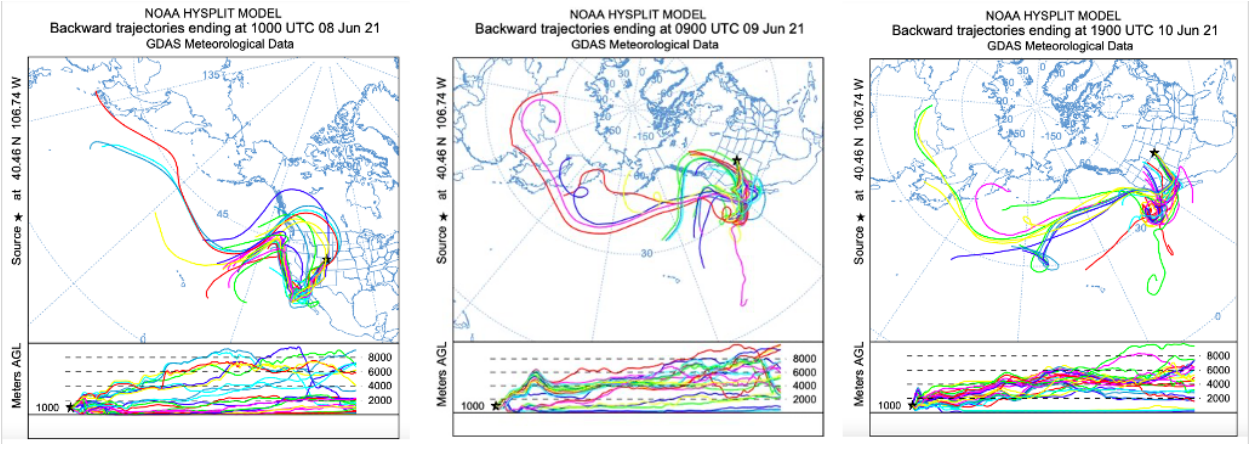

Event 5: June 12, 2021 11:00 MST - June 18, 2021 11:00 MST

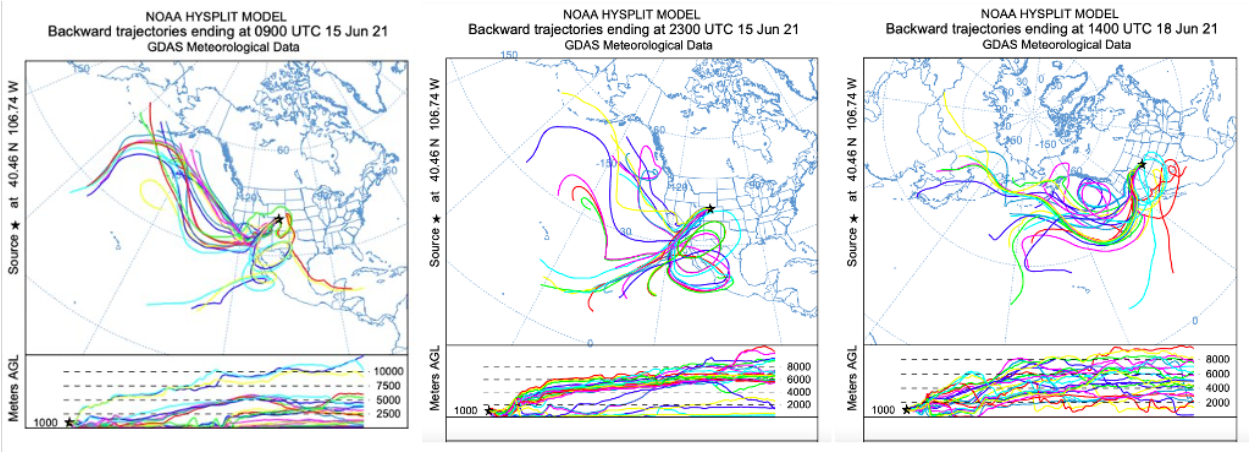

Event 6: August 11, 2021 06:00 MST - August 12, 2021 09:00 MST

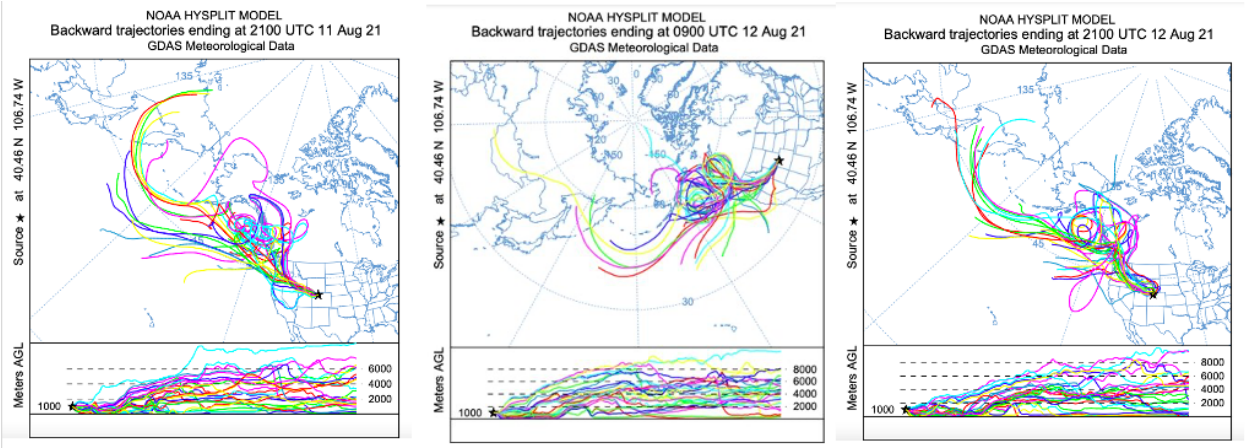

Event 7: August 23, 2021 01:00 MST - August 28, 2021 18:00 MST

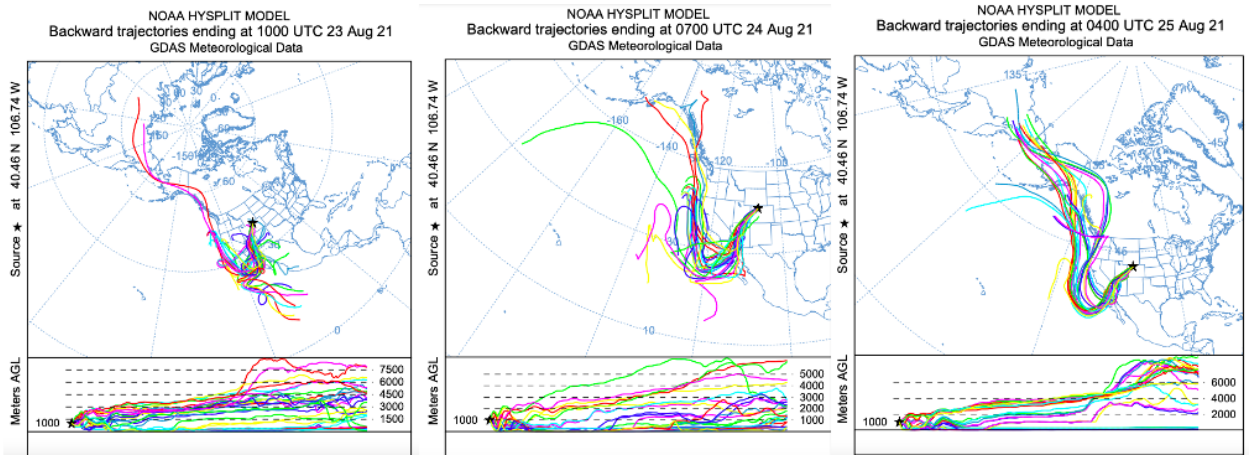

Event 8: September 6, 2021 05:00 MST - September 10, 2021 17:00 MST

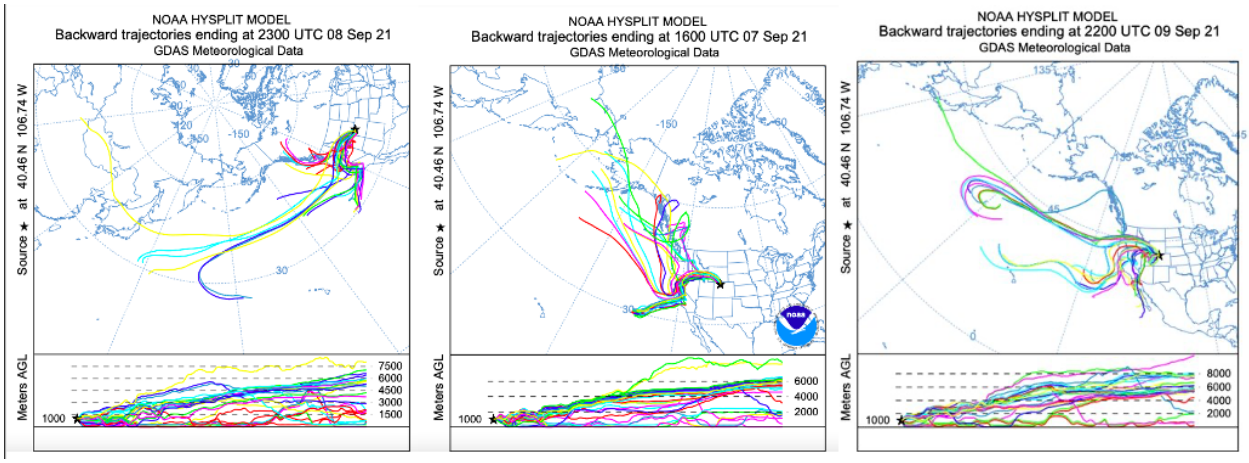

Event 9: September 13, 2021 22:00 MST - September 16, 2021 05:00 MST

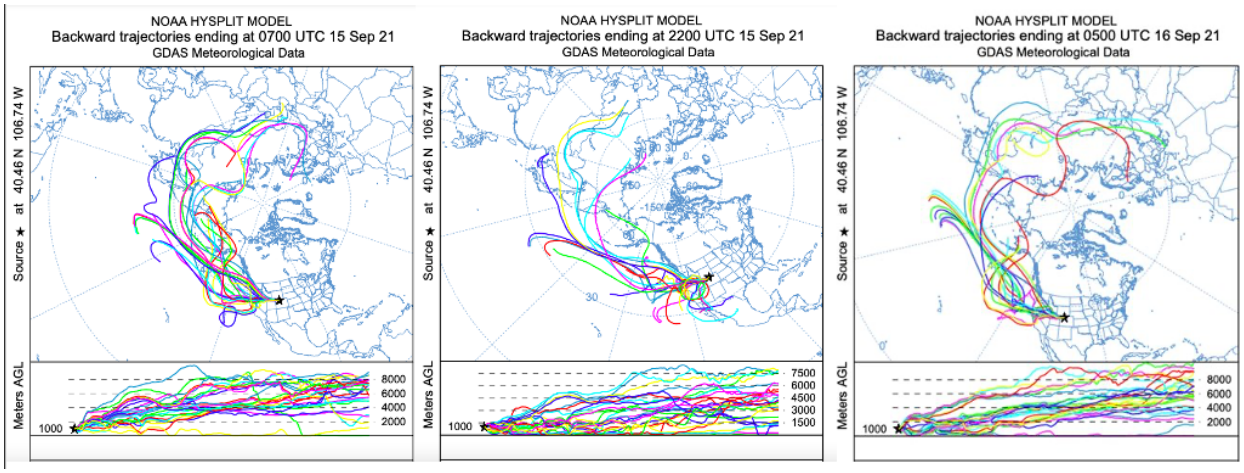

Event 13: May 6, 2022 09:00 MST - May 7, 2022 14:00 MST

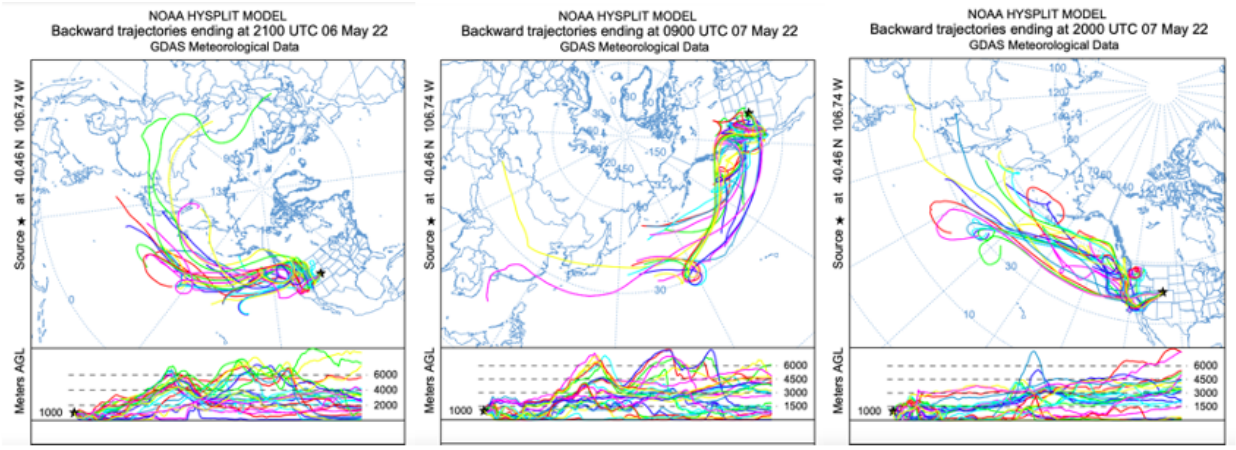

Event 15: May 26, 2022 07:00 MST - May 27, 2022 06:00 MST

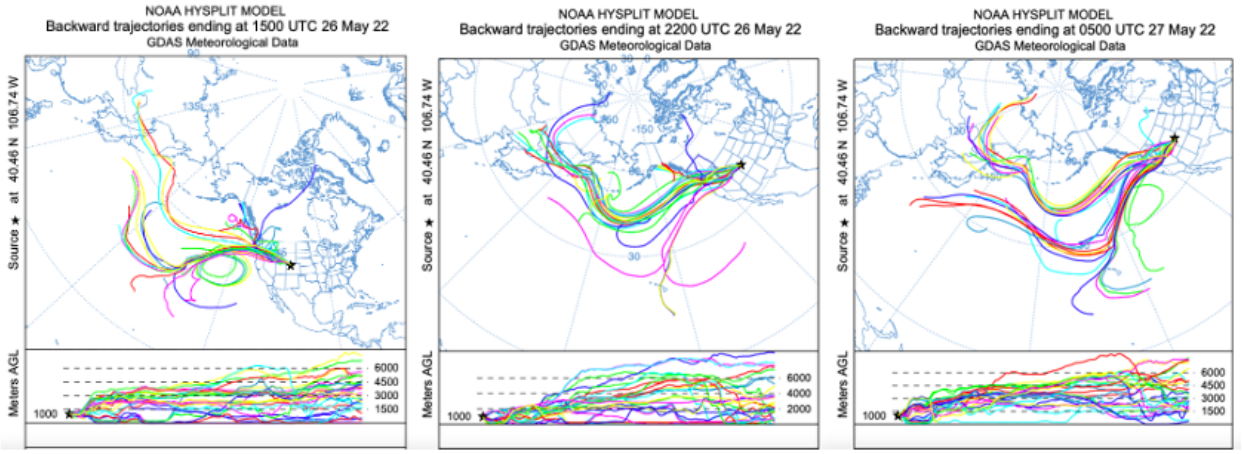

Event 17: June 10, 2022 12:00 MST - June 11, 2022 17:00 MST

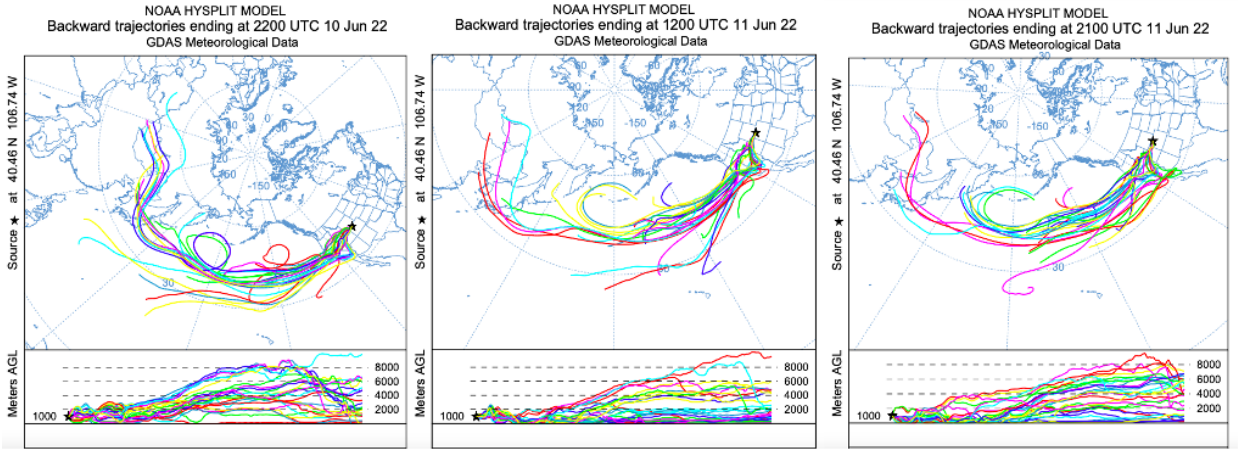

Event 21: July 20, 2022 19:00 MST - July 21, 2022 23:00 MST

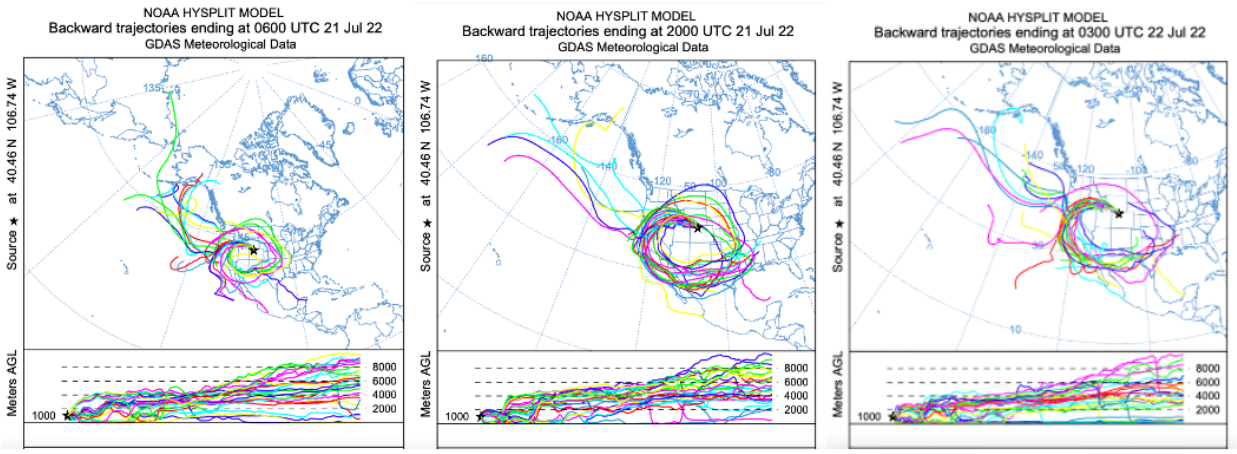

Event 22: September 12, 2022 06:00 MST - September 12, 2022 21:00

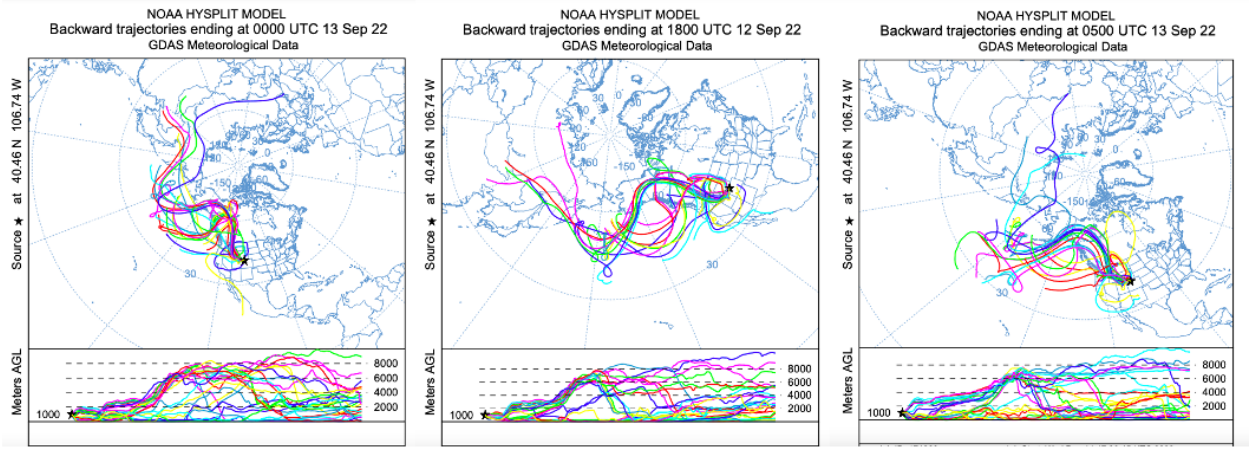

Figure 6: HYSPLIT GDAS Ensemble 10 Day Backwards Trajectories for Characterized Events. Model times in UTC.

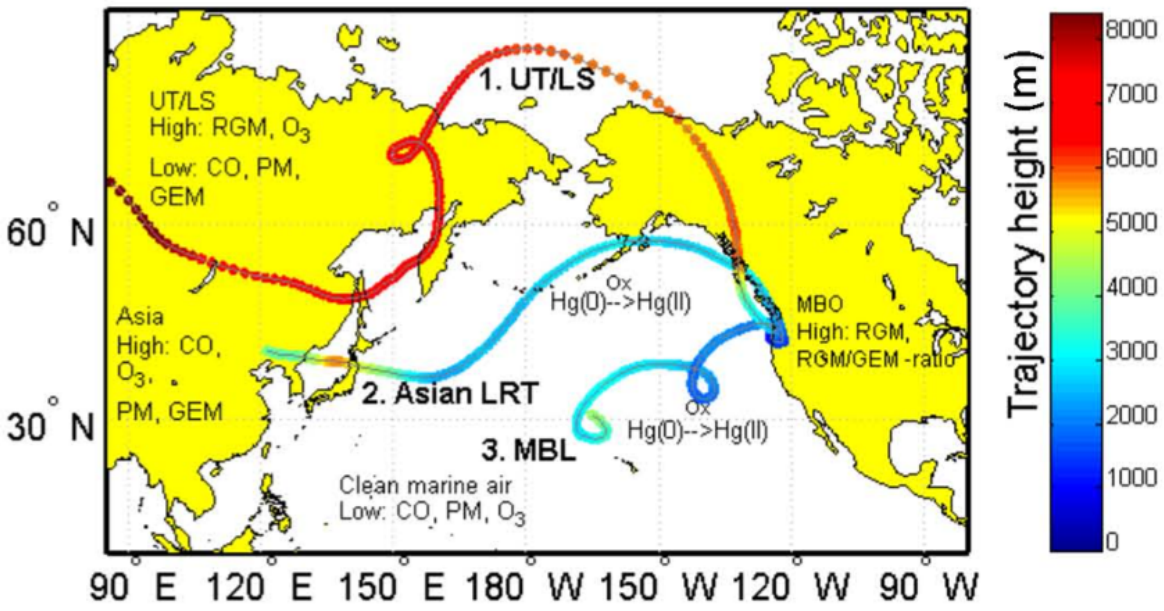

Figure 7: Example trajectories of three possible origins of Hg^{II} at MBO; UT/LS, ALRT, and MBL, identified by Timonen et al. (2013).

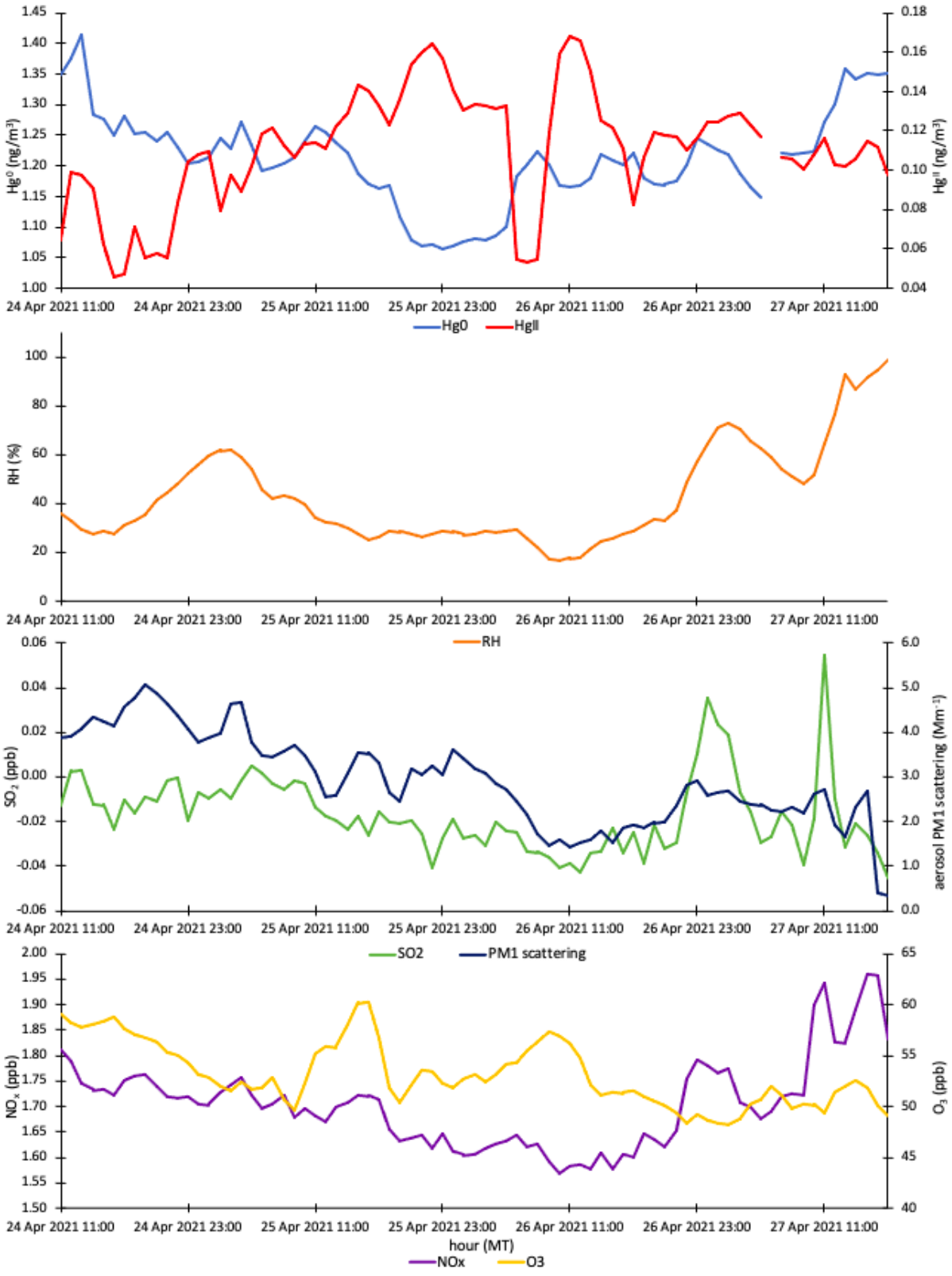

Figure 8: Event 2 Time Series of Hg, trace gases, relative humidity, and aerosol scattering.

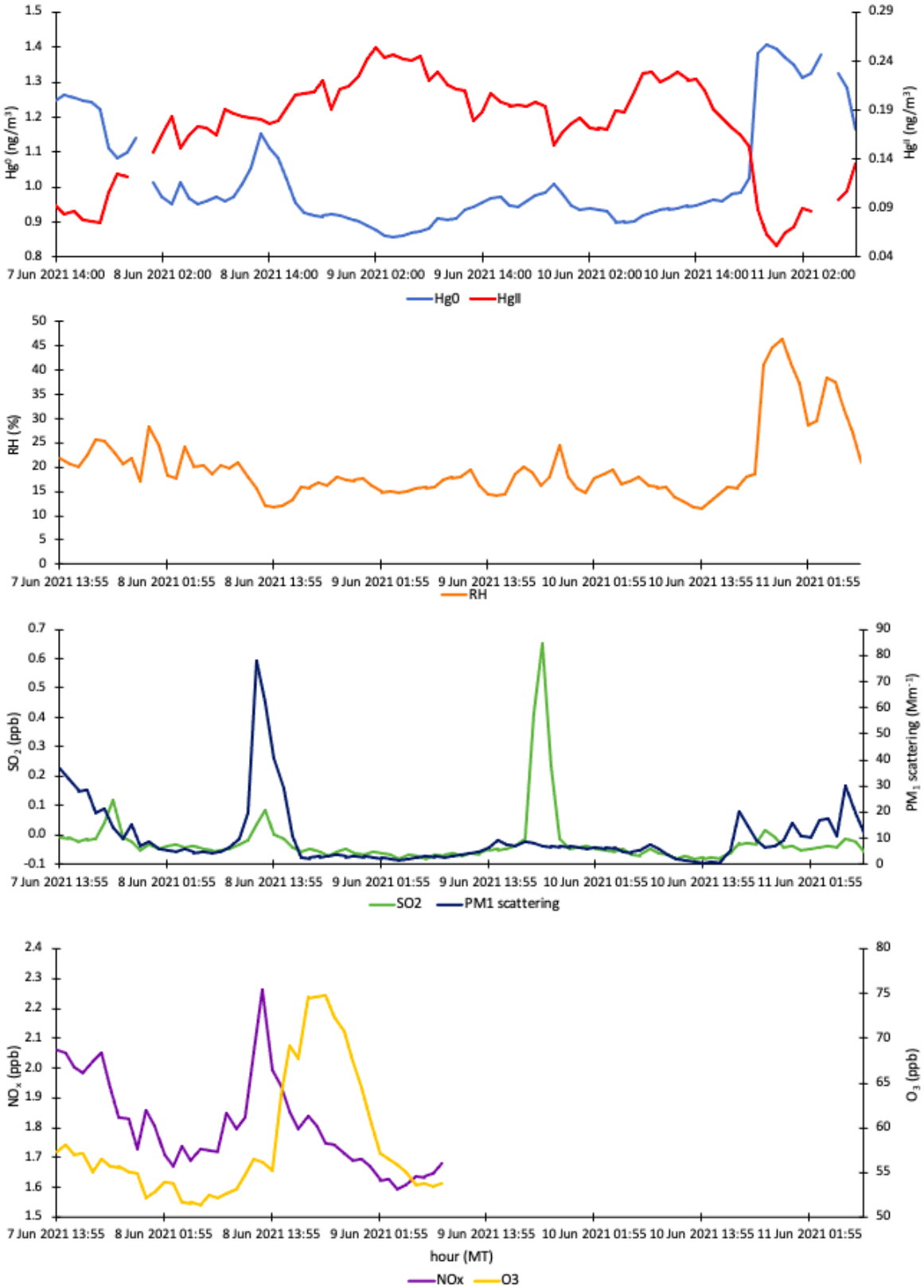

Figure 9: Event 4 Time Series of Hg, trace gases, relative humidity, and aerosol scattering.

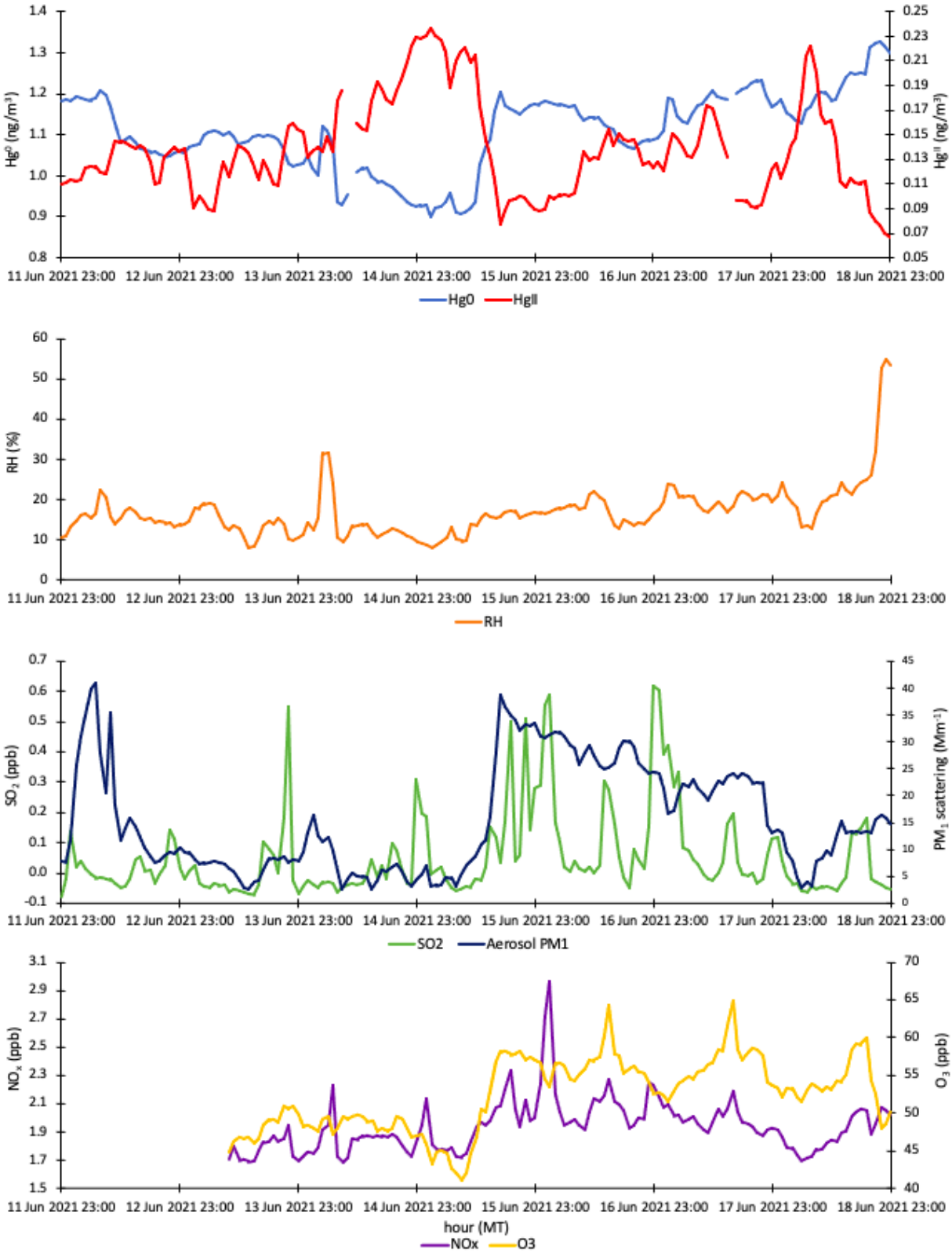

Figure 10: Event 5 Time Series of Hg, trace gases, relative humidity, and aerosol scattering.

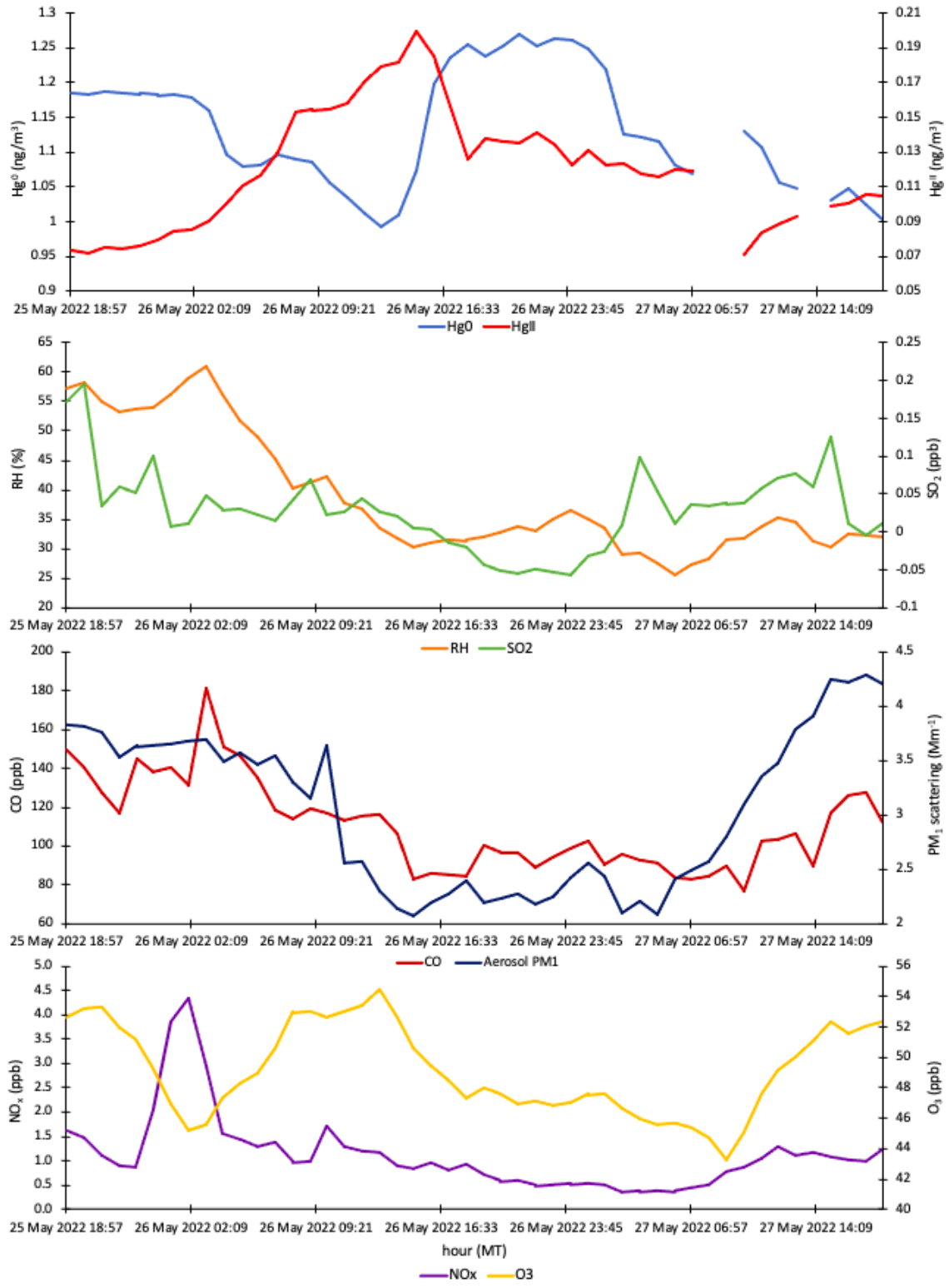

Figure 11: Event 15 Time Series of Hg, trace gases, relative humidity, and aerosol scattering.

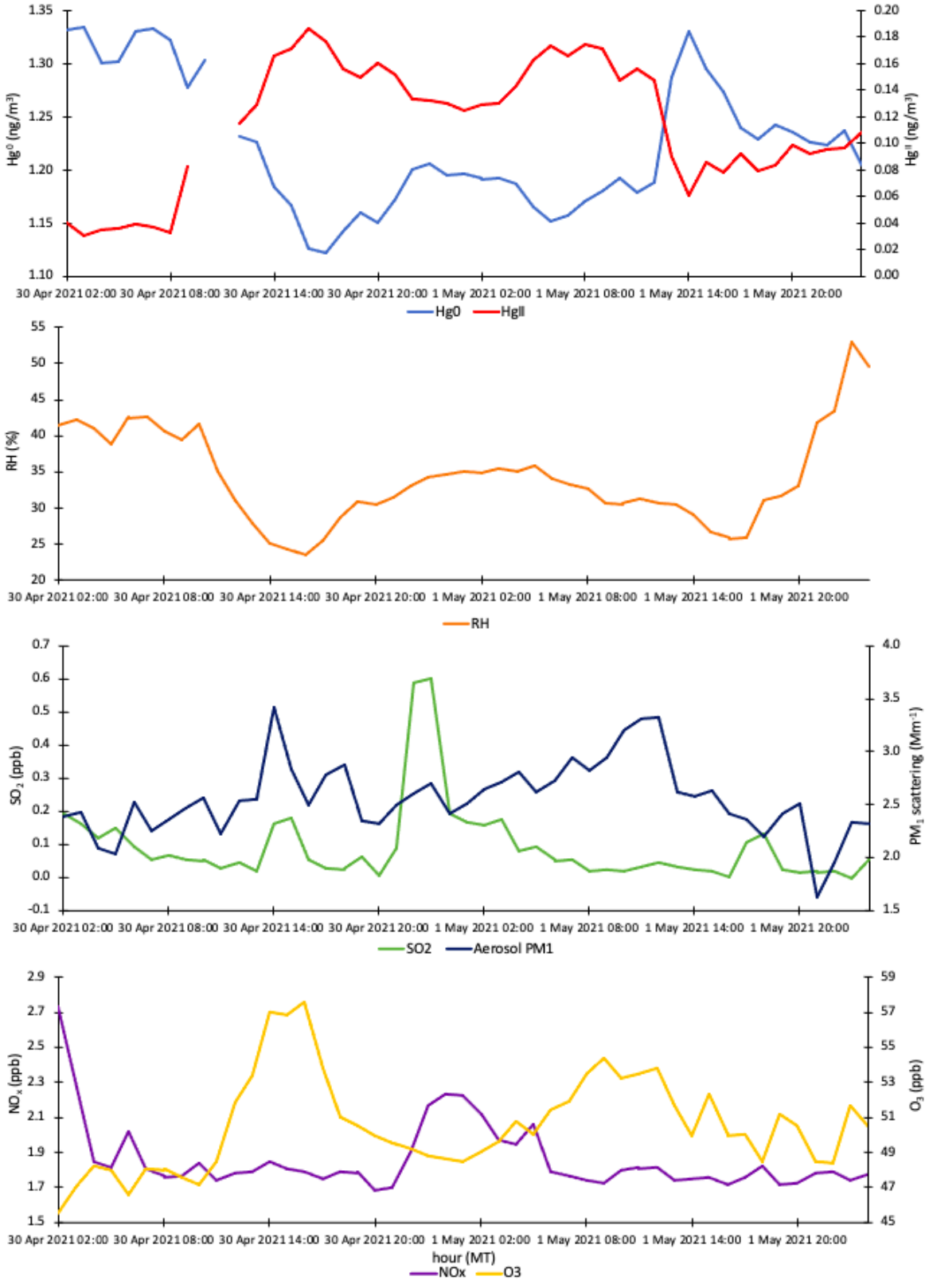

Figure 12: Event 3 Hg, trace gases, relative humidity, and aerosol scattering.

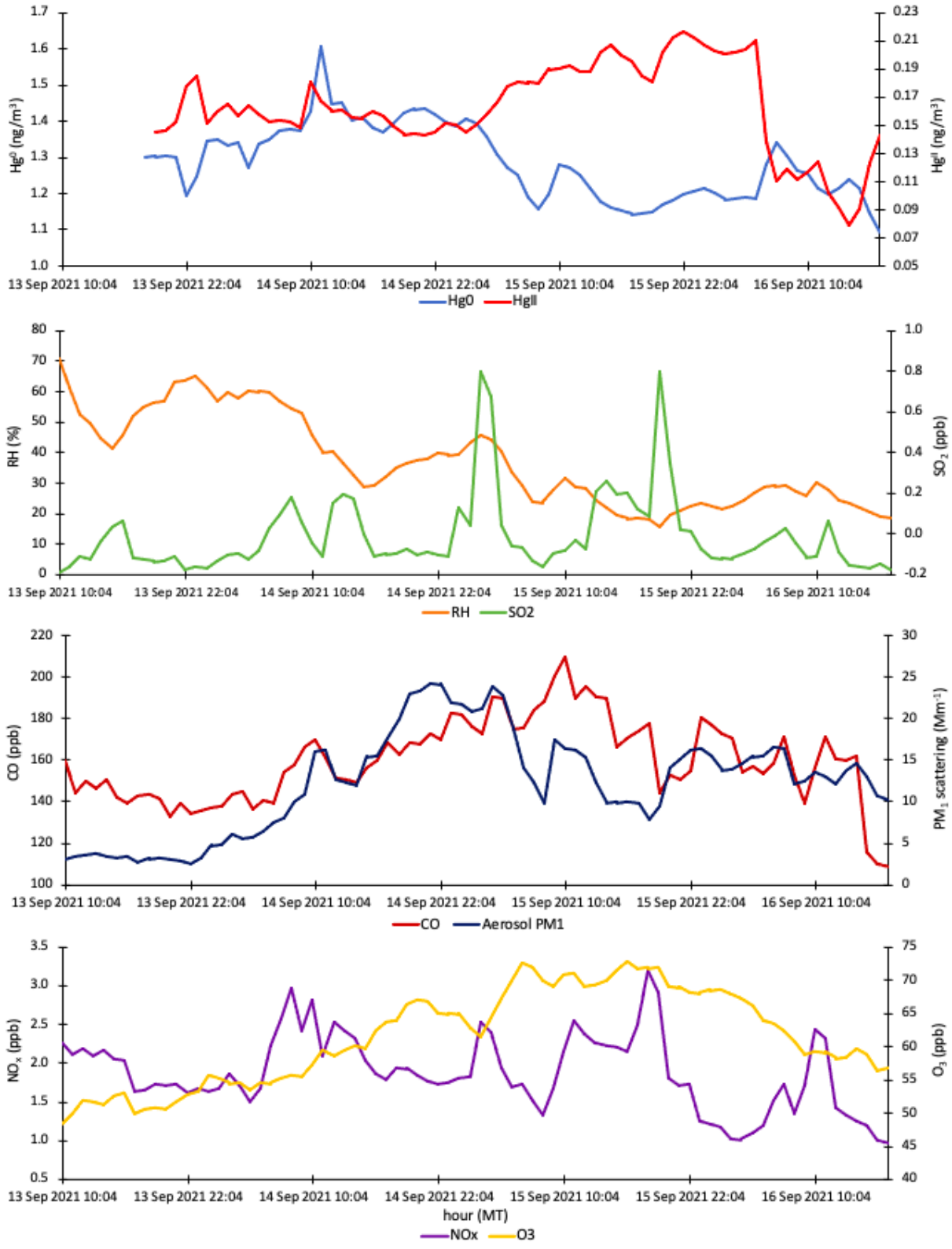

Figure 13: Event 9 Hg, trace gases, relative humidity, and aerosol scattering.

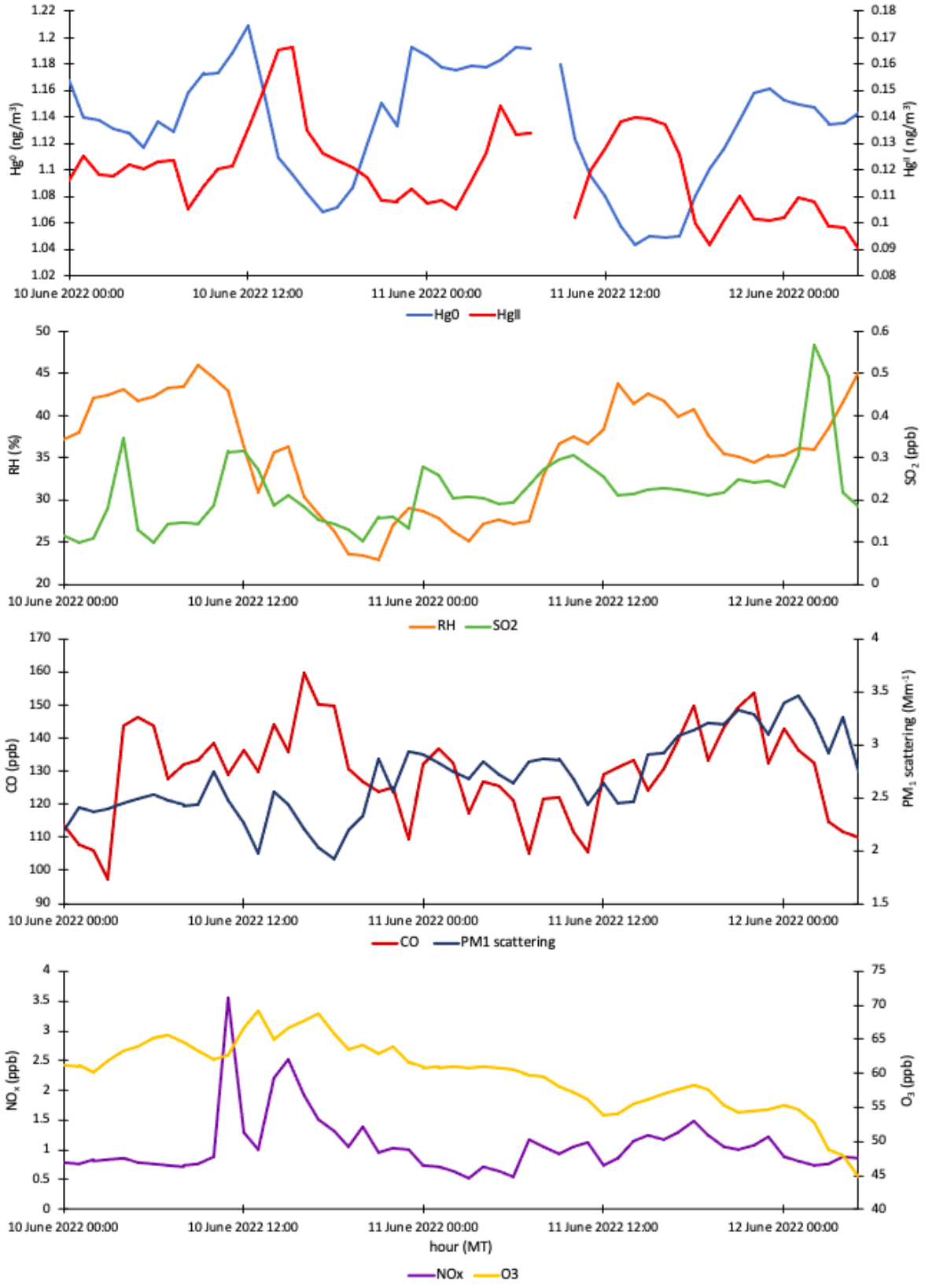

Figure 14: Event 17 Hg, trace gases, relative humidity, and aerosol scattering.

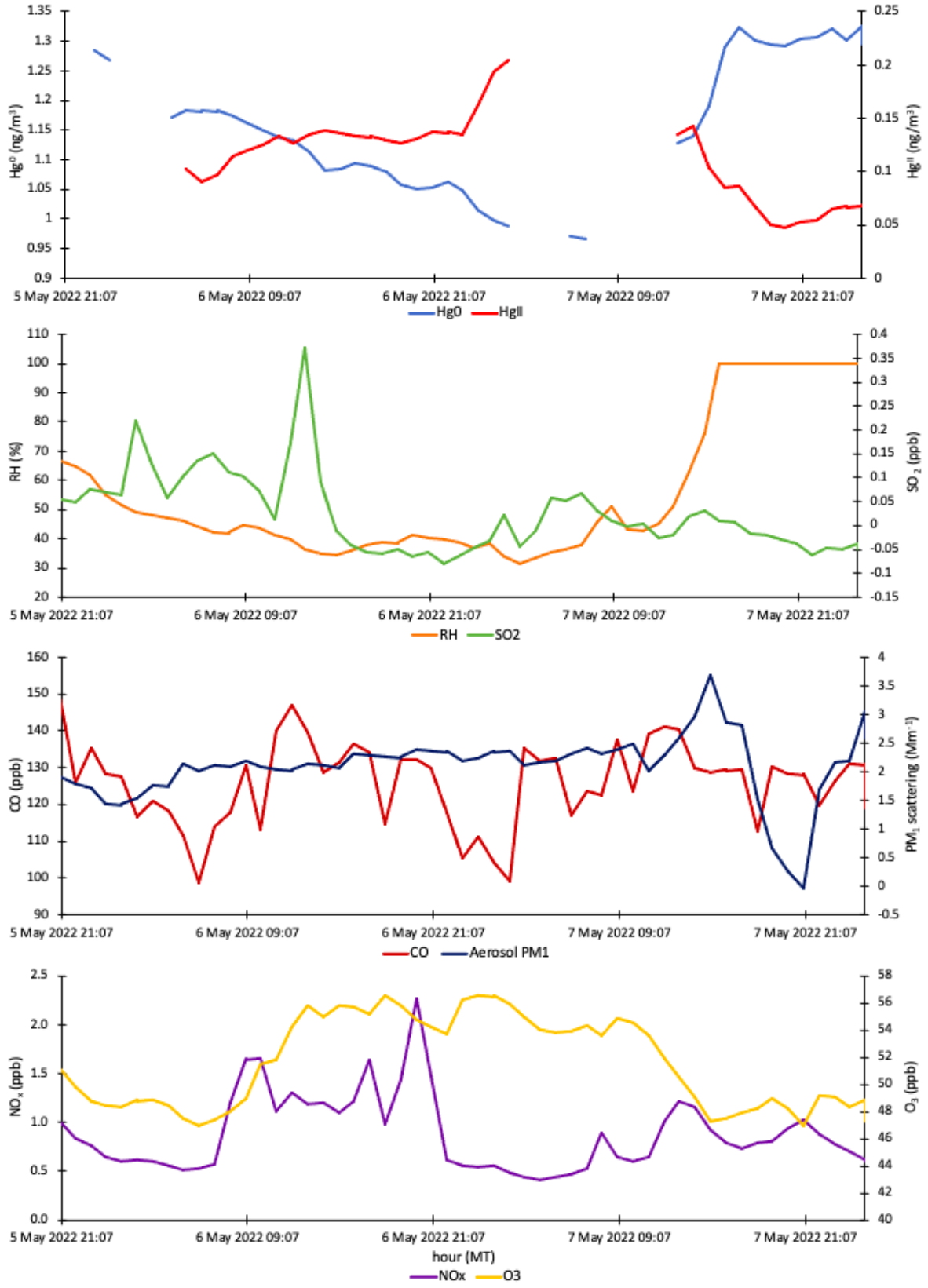

Figure 15: Event 13 Hg, trace gases, relative humidity, and aerosol scattering.

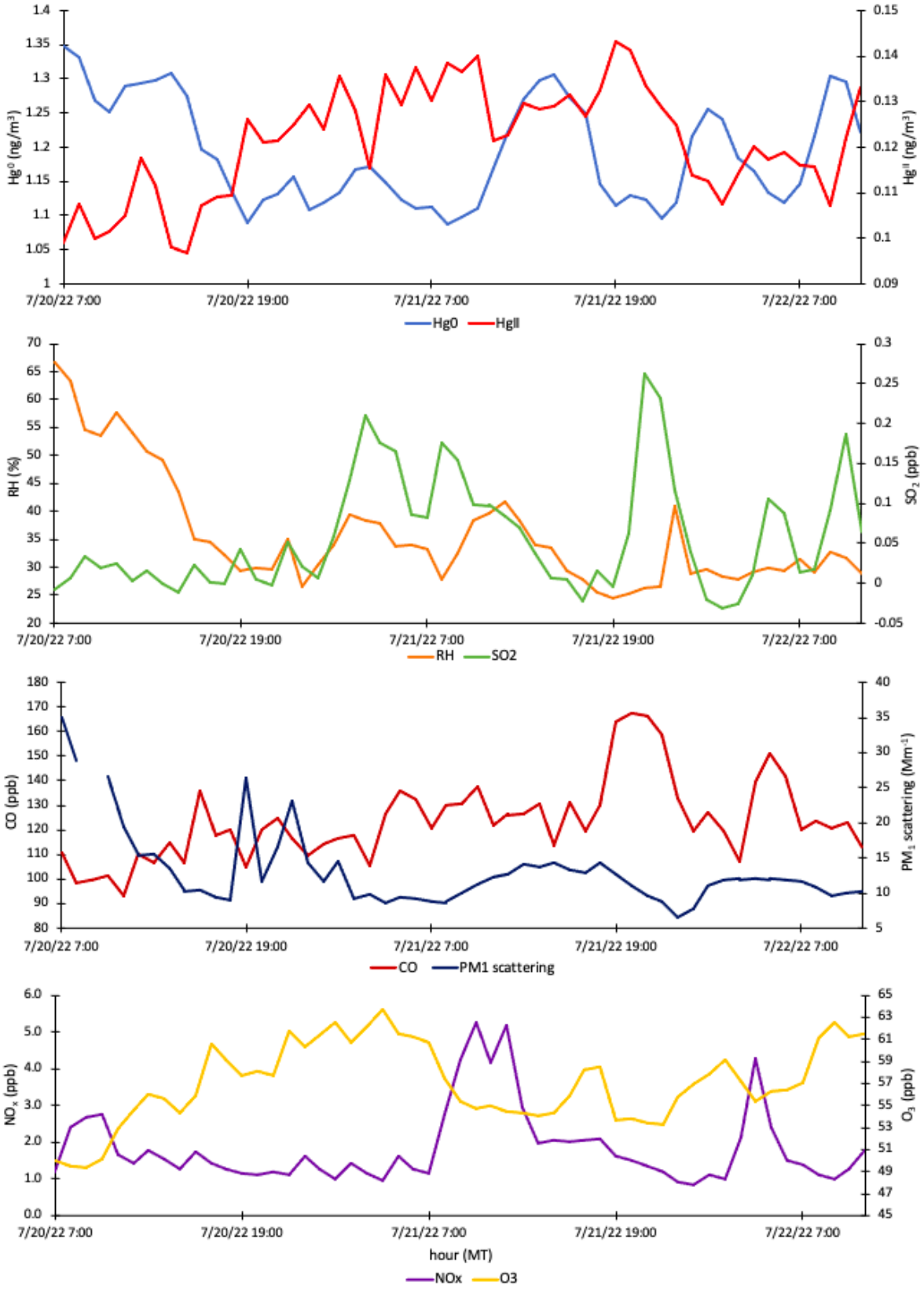

Figure 16: Event 21 Hg, trace gases, relative humidity, and aerosol scattering.

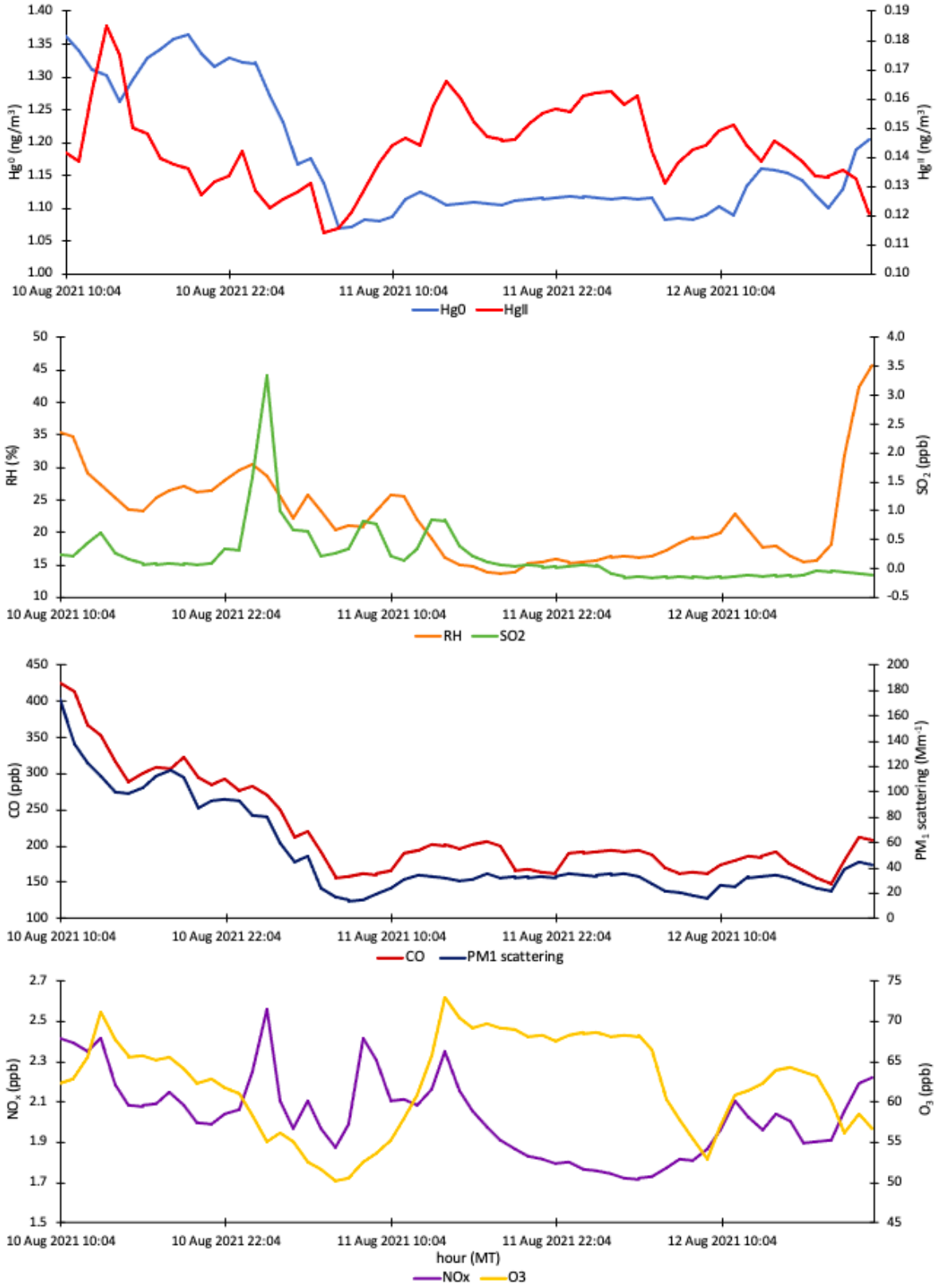

Figure 17: Event 6 Hg, trace gases, relative humidity, and aerosol scattering.

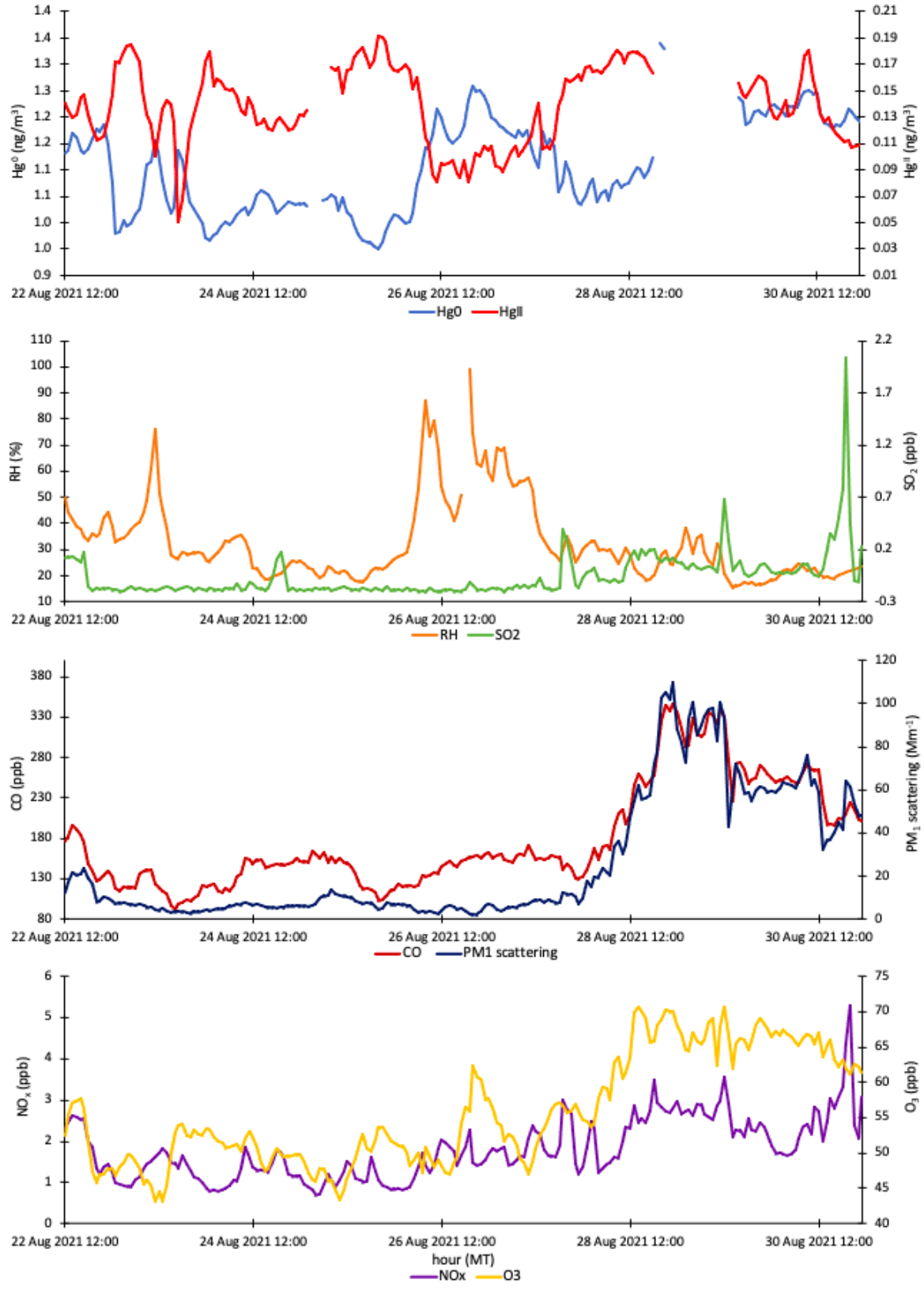

Figure 18: Event 7 Hg, trace gases, relative humidity, and aerosol scattering.

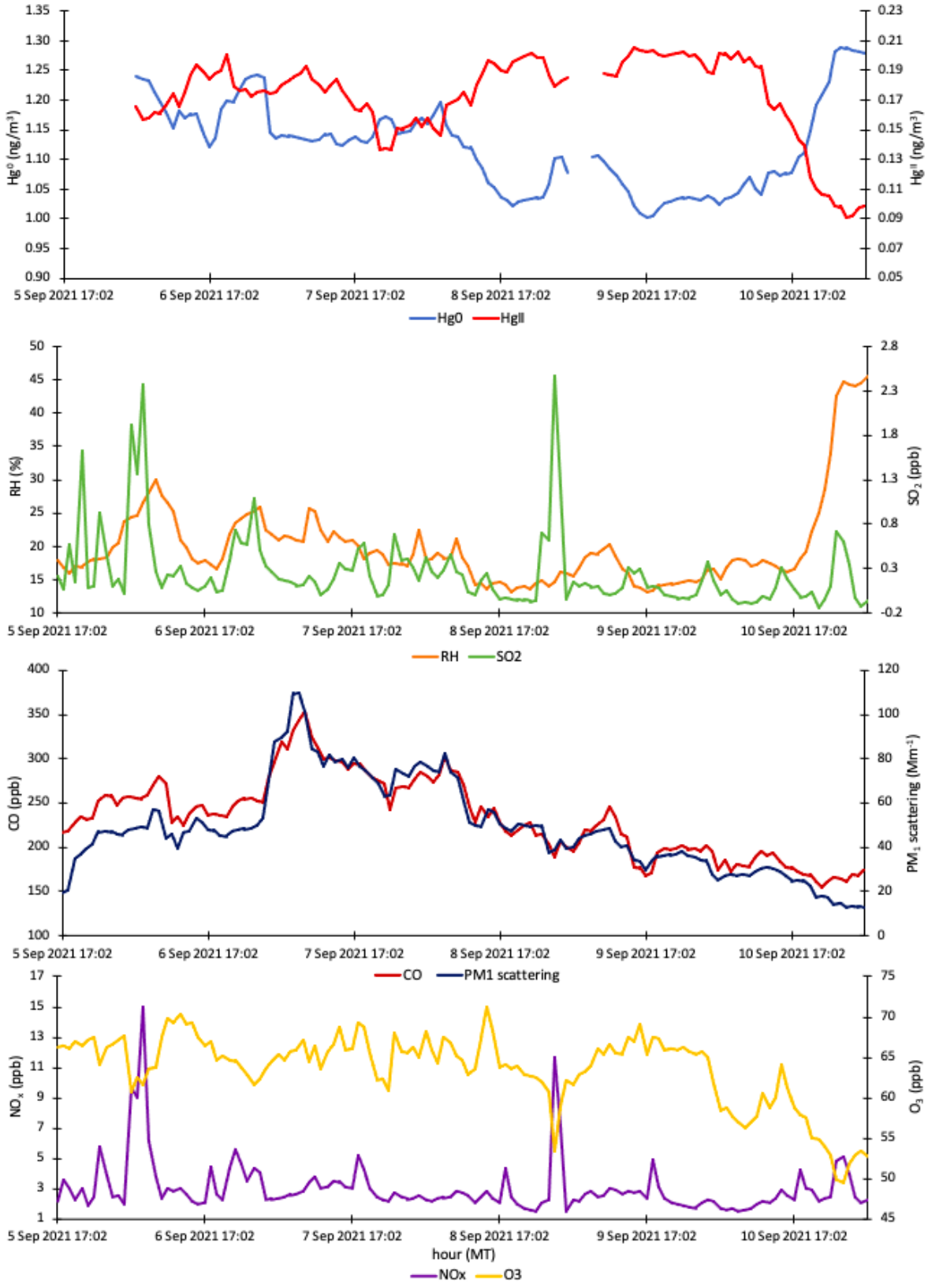

Figure 19: Event 8 Hg, trace gases, relative humidity, and aerosol scattering.

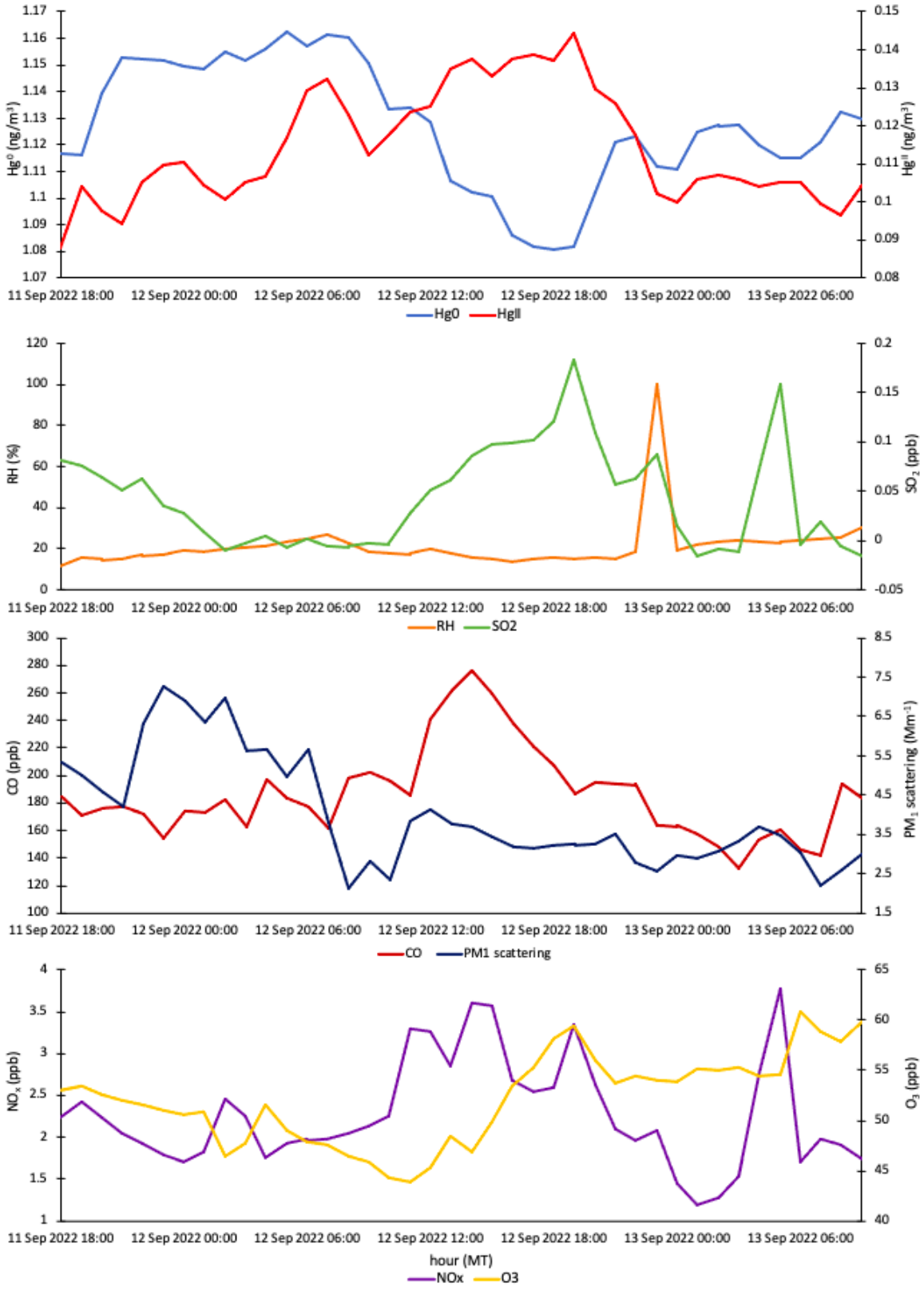

Figure 20: Event 22 Hg, trace gases, relative humidity, and aerosol scattering.

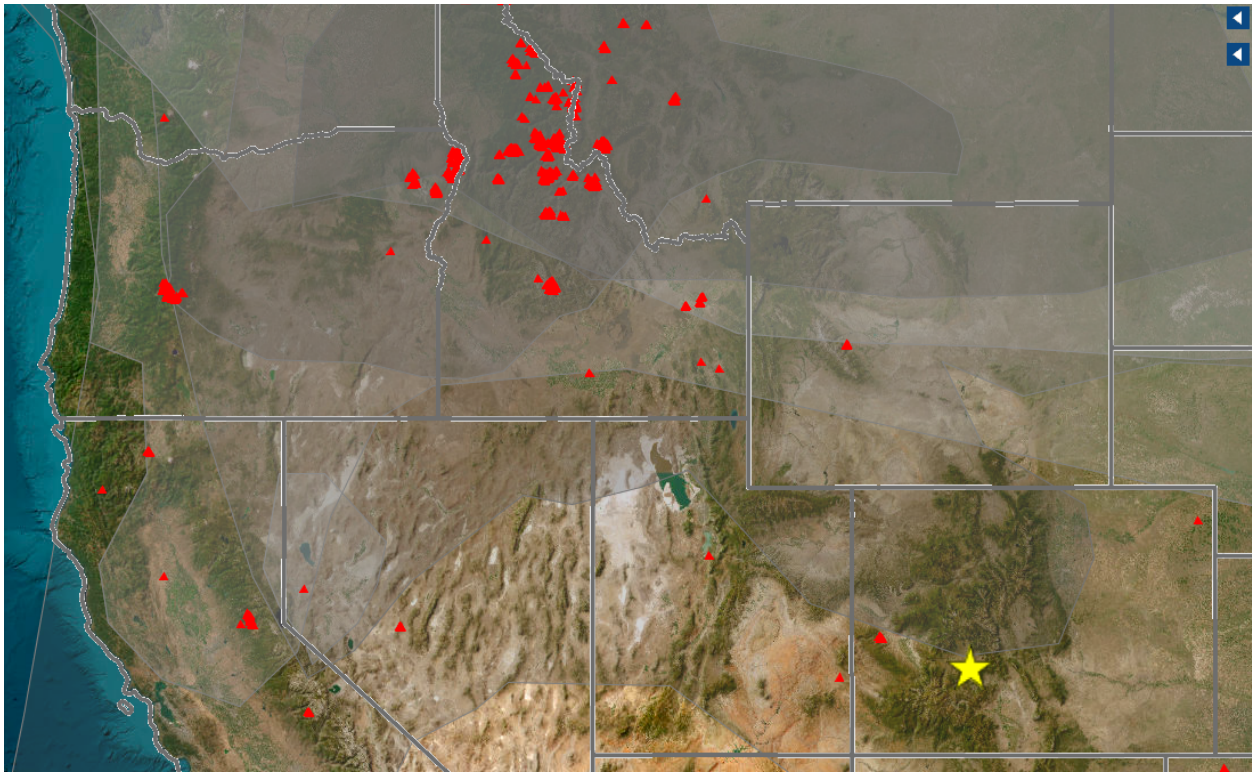

Figure 21: Overhead smoke map showing smoke at SPL on September 12, 2022 at 14:00 MST, midway through Event 22. Red triangles mark active fires, and shaded gray areas indicate the presence of overhead smoke. SPL is represented by the star.

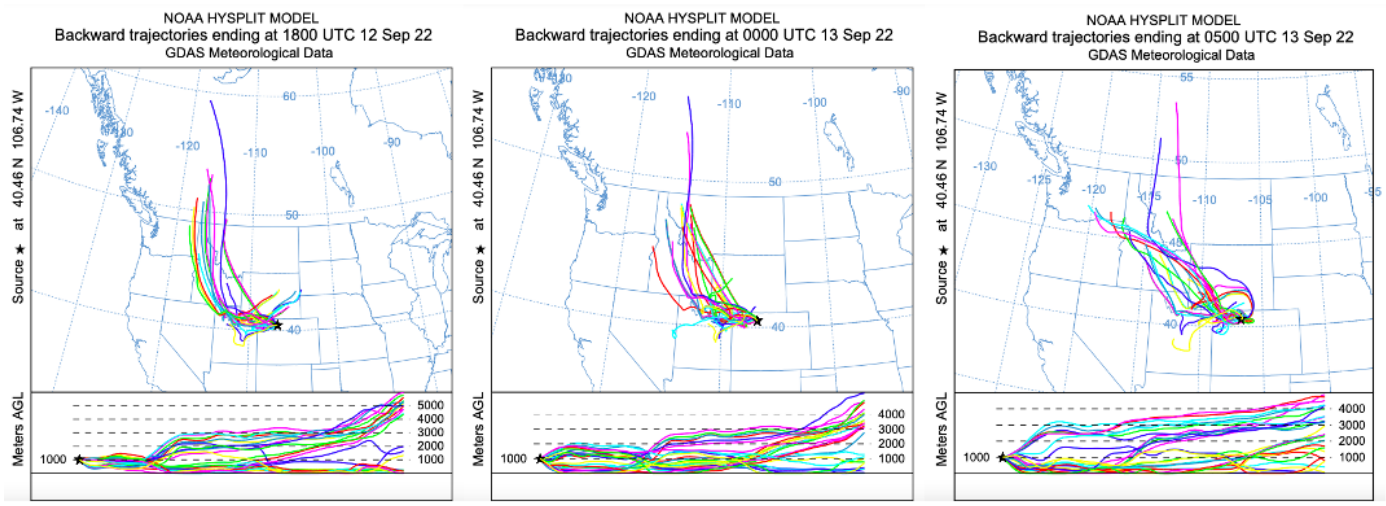

Figure 22: 3 day backwards HYSPLIT ensemble trajectories throughout Event 22

Tables:

Table 1. Spring 2021 Summary Statistics of Hg, Meteorology, and Criteria Gases

	Hg^{II} (pg/m^3)	Hg^0 (ng/m^3)	RH (%)	$PM_1\ \sigma_{sp}$ (Mm^{-1})	NO_x (ppb)	O_3 (ppb)	SO_2 (ppb)
Mean	79	1.3	62	3	1.9	48.1	0.01
Standard Deviation	51	0.1	26	2	0.2	8.5	0.1
Minimum	-50	1.0	15	0	1.2	18.0	-0.1
Maximum	520	2.1	100	10	3.2	69.1	1.1

Table 2. Summer 2021 Summary Statistics of Hg, Meteorology, and Criteria Gases

	Hg^{II} (pg/m^3)	Hg^0 (ng/m^3)	RH (%)	$PM_1\ \sigma_{sp}$ (Mm^{-1})	NO_x (ppb)	O_3 (ppb)	SO_2 (ppb)	CO (ppb)
Mean	120	1.2	45	30	2.0	57.5	0.02	201
Standard Deviation	42	0.1	25	40	0.4	93.5	0.2	93.5
Minimum	-2	0.9	7.8	-5.3	0.7	33.9	-0.2	80.7
Maximum	253	2.4	100	473.7	5.4	87.5	3.3	1858

Table 3. Spring 2022 Summary Statistics of Hg, Meteorology, and Criteria Gases

	Hg^{II} (pg/m^3)	Hg^0 (ng/m^3)	RH $(\%)$	PM_1 σ_{sp} (Mm^{-1})	NO_x (ppb)	O_3 (ppb)	SO_2 (ppb)	CO (ppb)
Mean	80	1.3	72	2.7	1.2	51.4	0.02	0.13
Standard Deviation	40	0.1	29	3.0	0.7	5.8	0.2	0.02
Minimum	3	0.8	18	-0.2	0.2	29.2	-0.2	0.07
Maximum	239	1.7	100	95	4.3	79.8	5.8	0.21

Table 4. Summer 2022 Summary Statistics of Hg, Meteorology, and Criteria Gases

	Hg^{II} (pg/m^3)	Hg^0 (ng/m^3)	RH $(\%)$	PM_1 σ_{sp} (Mm^{-1})	NO_x (ppb)	O_3 (ppb)	SO_2 (ppb)	CO (ppb)
Mean	86	1.3	55	3.9	1.2	52.1	0.03	122
Standard Deviation	3	0.1	23	4.8	0.6	6.3	0.2	20.8
Minimum	1	0.9	15	0.01	0.2	35.2	-0.5	42.3
Maximum	197	1.7	100	94.5	6.3	73.9	3.2	247

Table 5. Summary of 2021 Events of Elevated Oxidized Mercury

Season	Event #	Start Date (MST)	End Date (MST)
Spring	1	April 2 00:00	April 6 13:00
	2	April 24 23:00	April 27 05:00
	3	April 30 14:00	May 1 12:00
Summer	4	June 8 01:00	June 10 20:00
	5	June 12 11:00	June 18 11:00
	6	August 11 06:00	August 12 09:00
	7	August 23 01:00	August 28 18:00
	8	September 6 05:00	September 10 17:00
	9	September 13 22:00	September 16 05:00

Table 6. Summary of 2022 Events of Elevated Oxidized Mercury

Season	Event #	Start Date (MST)	End Date (MST)
Spring	10	March 3 10:00	March 4 17:00
	11	March 24 22:00	March 28 13:00
	12	April 27 03:00	April 28 04:00
	13	May 6 09:00	May 7 14:00
	14	May 10 10:00	May 12 04:00
	15	May 26 07:00	May 27 06:00
Summer	16	June 8 16:00	June 9 16:00
	17	June 10 12:00	June 11 17:00
	18	June 13 00:00	June 13 15:00
	19	June 16 05:00	June 17 03:00
	20	June 21 11:00	June 22 14:00
	21	July 20 19:00	July 21 23:00
	22	September 12 06:00	September 12 21:00 .

Table 7. Pearson Correlation Coefficients between Hg^{II} and Auxiliary Variables in 2021

	Hg^0	RH	PM_1 σ_{sp}	O_3	NO_x	SO_2	CO
Event 1	-0.54**	-0.45**	0.20*	-0.25**	-0.18*	0.24**	-
Event 2	-0.56**	-0.14	-0.39**	-0.26*	-0.32**	-0.18	-
Event 3	-0.95**	-0.57**	0.59**	0.71**	-0.22	-0.002	-
Event 4	-0.92**	-0.79**	-0.40**	0.24	-0.71**	-0.11	-
Event 5	-0.73**	-0.52**	-0.51**	-0.56**	-0.44**	-0.15*	-
Event 6	-0.08	-0.36**	0.08	0.77**	-0.08	-0.19	0.11
Event 7	-0.50**	-0.53**	0.26**	0.18*	-0.13	0.03	0.14
Event 8	-0.74**	-0.78**	0.20*	0.59**	-0.15	-0.10	0.13
Event 9	-0.31**	-0.16	-0.04	0.54**	0.09	0.17	0.34**

*p-value significance indicated by **<0.01; *<0.05*

Table 8. Pearson Correlation Coefficients between Hg^{II} and Auxiliary Variables in 2022

	Hg^0	RH	PM_1 σ_{sp}	O_3	NO_x	SO_2	CO
Event 10	0.03	0.38*	0.37*	0.24	-0.16	0.34*	0.09
Event 11	-0.57**	-0.41**	-0.67**	-0.25	-0.19	-0.47**	-0.19
Event 12	-0.41**	-0.13	0.25	0.07	-0.20	-0.17	0.36*
Event 13	-0.93**	-0.84**	0.42**	0.78**	0.15	0.11	-0.17
Event 14	-0.76**	-0.63**	-0.48**	0.04	-0.57**	0.53**	-0.20
Event 15	-0.16	-0.52**	-0.66**	0.20	-0.33*	-0.44**	-0.45**
Event 16	-0.40**	0.18	-0.30	-0.16	-0.10	-0.04	0.06
Event 17	-0.24	-0.05	-0.50**	0.49**	0.35	-0.14	0.11
Event 18	-0.88**	0.56**	0.09	-0.17	0.35*	0.29	-0.10
Event 19	-0.51**	0.49**	-0.41**	-0.29*	0.41**	-0.20	0.32*
Event 20	-0.57**	-0.58**	0.18	-0.08	-0.17	0.22	0.07
Event 21	-0.60**	-0.58**	-0.34*	0.29*	0.16	0.43**	0.57**
Event 22	-0.44**	-0.21	-0.22	-0.18	0.52**	0.41**	0.64**

*p-value significance indicated by **<0.01; *<0.05*

Table 9. Means and Standard Deviations for Events Characterized in this Study

	Hg^{II} (pg/m^3)	Hg^0 (ng/m^3)	RH (%)	$PM_1\ \sigma_{sp}$ (Mm^{-1})	NO_x (ppb)	O_3 (ppb)	SO_2 (ppb)	CO (ppb)
Clean Air Events								
Event 2	121 ± 25	1.2 ± 0.1	38 ± 16	2.8 ± 0.8	1.7 ± 0.1	53 ± 3	-0.02 ± 0.02	-
Event 4	200 ± 26	0.9 ± 0.0	17 ± 3	6.9 ± 10.2	1.7 ± 0.1	59 ± 8	-0.03 ± 0.11	-
Event 5	143 ± 38	1.1 ± 0.1	16 ± 4	14.8 ± 10.0	2.0 ± 0.2	52 ± 5	0.06 ± 0.15	-
Event 15	145 ± 24	1.1 ± 0.1	34 ± 5	3.0 ± 0.7	0.8 ± 0.4	49 ± 3	0.03 ± 0.05	100 ± 10
Elevated Ozone								
Event 3	154 ± 18	1.2 ± 0.0	31 ± 4	2.8 ± 0.3	1.9 ± 0.2	52 ± 3	0.13 ± 0.16	-
Event 9	175 ± 22	1.3 ± 0.1	36 ± 14	14.0 ± 5.8	1.9 ± 0.5	64 ± 6	0.03 ± 0.22	170 ± 20
Event 13	140 ± 22	1.1 ± 0.1	40 ± 5	2.1 ± 0.6	1.0 ± 0.5	54 ± 2	0.02 ± 0.08	130 ± 10
Event 17	119 ± 17	1.1 ± 0.0	36 ± 7	2.7 ± 0.4	1.1 ± 0.5	60 ± 5	0.22 ± 0.09	130 ± 10
Event 21	121 ± 12	1.2 ± 0.1	36 ± 10	13.2 ± 5.5	1.9 ± 1.0	57 ± 4	0.06 ± 0.07	120 ± 20
Combustion Tracer Influence								
Event 6	148 ± 13	1.1 ± 0.0	18 ± 3	28.4 ± 7.4	1.9 ± 0.2	63 ± 7	0.17 ± 0.32	180 ± 20
Event 7	140 ± 32	1.1 ± 0.1	36 ± 17	10.5 ± 12.5	1.5 ± 0.5	52 ± 6	-0.13 ± 0.11	150 ± 30
Event 8	180 ± 17	1.1 ± 0.1	19 ± 4	53.1 ± 19.7	3.1 ± 1.9	64 ± 3	0.26 ± 0.43	240 ± 40
Event 22	114 ± 15	1.1 ± 0.0	22 ± 13	4.0 ± 1.4	2.3 ± 0.6	52 ± 4	0.04 ± 0.05	190 ± 30

References

Castro, P. J., Kellö, V., Cernušák, I., & Dibble, T. S. (2022). Together, Not Separately, OH and O 3 Oxidize Hg (0) to Hg (II) in the Atmosphere. *The Journal of Physical Chemistry*. A, 126(44), 8266–8279. https://doi-org.coloradocollege.idm.oclc.org/10.1021/acs.jpca.2c04364.

Dibble, T. S., Tetu, H. L., Jiao, Y., Thackray, C. P., Jacob, D. J. (2020). Modeling the OH-Initiated Oxidation of Mercury in the Global Atmosphere without Violating Physical Laws. *The Journal of Physical Chemistry*. A, 124, 444-453. doi:10.1021/acs.jpca.9b10121.

Driscoll, C. T., Mason, R. P., Chan, H.M., Jacob, D. J., & Pirrone, N. (2013). Mercury as a global pollutant: Sources, pathways, and effects. *Environmental Science & Technology, 47*(10), 4967-4983. doi:10.1021/es305071v.

EPA. (2022, April 14). *Health Effects of Exposure to Mercury*. United States Environmental Protection Agency. https://www.epa.gov/mercury/health-effects-exposures-mercury.

Faïn, X., Obrist, D., Hallar, A.G., Mccubbin, I., Rahn, T. (2009). High levels of reactive gaseous mercury observed at a high elevation research laboratory in the Rocky Mountains. *Atmospheric Chemistry and Physics, 9: 8049-8060*. www.atmos-chem-phys.net/9/8049/2009/.

Finley, B.D., Swartzendruber, P.C., Jaffe, D.A. (2009). Particulate mercury emissions in regional wildfire plumes observed at the Mount Bachelor Observatory. *Atmospheric Environment*, *43*(38), 6074–6083. https://doi.org/10.1016/j.atmosenv.2009.08.046.

Friedli, H., Radke, L., Lu, J., Banic, C., Leaitch, W., & MacPherson, J. (2003). Mercury emissions from burning of biomass from temperate North American forests: laboratory and airborne measurements. *Atmospheric Environment*, *37*(2), 253–267. https://doi-org.coloradocollege.idm.oclc.org/10.1016/S1352-2310(02)00819-1.

Gratz, L., Ambrose, J., Jaffe, D., Shah, V., Jaeglé, L., Stutz, J., Festa, J., Spolaor, M., Tsai, C., Selin, N., Song, S., Zhou, X., Weinheimer, A., Knapp, D. J., Montzka, D. D., Flocke, F., Campos, T., Apel, E. C., Hornbrook, R. S., Blake, N., Hall, S., Tyndall, G., Reeves, M., Stechman, D., Stell, M., (2015). Oxidation of mercury by bromine in the subtropical Pacific free troposphere. *Geophys.Res.Lett.42, 10494–10502.*

Lyman, S. N., Gustin, M. S., Prestbo, E. M., Marsik, F. J. (2007). Estimation of dry deposition of atmospheric mercury in Nevada by direct and indirect methods. *Environ.Sci.Technol.41,1970–1976. Doi:* 10.1021/es062323m.

Lyman, S. N. and Jaffe, D. A. (2011). Formation and fate of oxidized mercury in the upper troposphere and lower stratosphere. *Nature: Geoscience, 5: 114-117*. doi: 10.1038/NGEO1353.

Lyman, S. N., Gratz, L. E., Dunham-Cheatham, S. M., Gustin, M. S. and Luippold, A. (2020). Improvements to the Accuracy of Atmospheric Oxidized Mercury Measurements, Environ. Sci. Technol., 54, 13379, 10.1021/acs.est.0c02747.

Mao, H., Cheng, I., Zhang, L. (2016). Current understanding of the driving mechanisms for spatio temporal variations of atmospheric speciated mercury: a review. *Atmos.Chem.Phys.16, 12897–12924.* https://doi.org/10.5194/acp-16-12897-2016, 2016.

McLagan, D. S., Stupple, G. W., Darlington, A., Hayden, K., & Steffen, A. (2021). Where there is smoke there is mercury: Assessing boreal forest fire mercury emissions using aircraft and highlighting uncertainties associated with upscaling emissions estimates. *Atmospheric Chemistry & Physics*, *21*(7), 5635–5653. https://doi-org.coloradocollege.idm.oclc.org/10.5194/acp-21-5635-2021.

National Oceanic and Atmospheric Administration. (n.d.). *Atmospheric Mercury*. Air Resources Laboratory. Retrieved April 7, 2023, from https://www.arl.noaa.gov/research/surface-atmosphere-exchange-home/sae-programs-mercury/.

Obrist, D., Kirk, J. L., Zhang, L., Sunderland, E. M., Jiskra, M., & Selin, N. E. (2018). A review of global environmental mercury processes in response to human and natural perturbations : Changes of emissions, climate, and land use. *Ambio*, *47*(2), 116–140.

Schuster, F. P., Naftz, L. D., Cecil, D. L., Olson, L. M., Dewild, J. F., Susong, D. D., Green, J. R., Abbott, L. M. (2002). Atmospheric mercury deposition during the last 270 years: A glacial ice core record of natural and anthropogenic sources. *Environ. Sci. Technol.* 2002, 36, 11, 2303–2310. https://doi.org/10.1021/es0157503.

Selin, N.E., 2009. Global Biogeochemical Cycling of Mercury: A Review. *Annual Review of Environment and Resources 34, 43-63*. doi: 10.1146/annurev.environ.051308.084314

Shah, V., Jaeglé, L., Gratz, L., Ambrose, J., Jaffe, D., Selin, N., Song, S., Campos, T., Flocke, F., Reeves, M., Stechman, D., Stell, M., Festa, J., Stutz, J., Weinheimer, A., Knapp, D. J., Montzka, D. D., Tyndall, G., Apel, E. C., Hornbrook, R. S., Hills, A. J., Riemer, D. D., Blake, N., Cantrell, C. A., Mauldin,R.L (2016). Origin of oxidized mercury in the summertime free troposphere over the southeastern *US.Atmos.Chem.Phys.16,1511–1530.* doi:10.5194/acp-16-1511-2016.

Sprovieri, F., Pirrone, N., Bencardino, M., D'Amore, F., Carbone, F., Cinnirella, S., Mannarino, V., Landis, M., Ebinghaus, R., Weigelt, A., Brunke, E. G., Labuschagne, C., Martin, L., Munthe, J., Wangberg, I., Artaxo, P., Morais, F., Barbosa, H. M., Brito, J., Cairns, W., Barbante, C., Dieguez, M. C., Garcia, P. E., Dommergue, A., Angot, H., Magand, O., Skov, H., Horvat, M., Kotnik, J., Read, K. A., Neves, L. M., Gawlik, B. M., Sena, F., Mashyanov, N., Obolkin, V., Wip, D., Feng, X. B., Zhang, H., F, X., Ramachandran, R., Cossa, D.,Knoery, J., Marusczak, N., Nerentorp, M., Norstrom, C. (2016). Atmospheric mercury concentrations observed at ground-based monitoring sites globally distributed in

the framework of the GMOS network. *Atmos. Chem. Phys. 16, 11915–11935.* doi: 10.5194/acp-16-11915-2016

Sundseth, K., Pacyna, J. M., Pacyna, E. G., Munthe, J., Belhaj, M., Astrom, S. (2010). Economic benefits from decreased mercury emissions: Projections for 2020. *J.Clean.Prod. 2010*, 18, 386−394. doi: 10.3390/ijerph14010105.

Swartzendruber, P. C., Jaffe, D. A., Prestbo, E. M., Weiss-Penzias, P., Selin, N. E., Park, R., Jacob, D. J., Strode, S., Jaeglé, L. (2006), Observations of reactive gaseous mercury in the free troposphere at the Mount Bachelor Observatory, *J. Geophys. Res.*, 111, D24301, doi:10.1029/2006JD007415.

Timonen, H., Ambrose, J.L., Jaffe, D. A. (2013). Oxidation of elemental Hg in anthropogenic and marine airmasses. *Atmospheric Chemistry and Physics, 13: 2827-2836*. doi:10.5194/acp-13-2827-2013.

United Nations. (2022). *Minamata Convention on Mercury*. United Nations Treaty Collection. https://treaties.un.org/Pages/ViewDetails.aspx?src=IND&mtdsg_no=XXVII-17&chapter=27&clang=_en.

Zwecker, Z. (2021). Observations of ambient mercury from Storm Peak Laboratory using an improved dual-channel measurement system. [Senior Thesis]. Colorado College.